J. Fluid Mech. (2014), *vol.* 749, *pp.* 331–366.
doi:10.1017/jfm.2014.228

On cumulative nonlinear acoustic waveform distortions from high-speed jets

W. J. Baars[1,†], C. E. Tinney[1], M. S. Wochner[2,‡] and M. F. Hamilton[2]

[1]Department of Aerospace Engineering & Engineering Mechanics, University of Texas at Austin, Austin, TX 78712, USA

[2]Applied Research Laboratories, University of Texas at Austin, Austin, TX 78713, USA

(Received 21 October 2012; revised 2 April 2014; accepted 21 April 2014; first published online 19 May 2014)

A model is proposed for predicting the presence of cumulative nonlinear distortions in the acoustic waveforms produced by high-speed jet flows. The model relies on the conventional definition of the acoustic shock formation distance and employs an effective Gol'dberg number Λ for diverging acoustic waves. The latter properly accounts for spherical spreading, whereas the classical Gol'dberg number Γ is restricted to plane wave applications. Scaling laws are then derived to account for the effects imposed by jet exit conditions of practical interest and includes Mach number, temperature ratio, Strouhal number and an absolute observer distance relative to a broadband Gaussian source. Surveys of the acoustic pressure produced by a laboratory-scale, shock-free and unheated Mach 3 jet are used to support findings of the model. Acoustic waveforms are acquired on a two-dimensional grid extending out to 145 nozzle diameters from the jet exit plane. Various statistical metrics are employed to examine the degree of local and cumulative nonlinearity in the measured waveforms and their temporal derivatives. This includes a wave steepening factor (WSF), skewness, kurtosis and the normalized quadrature spectral density. The analysed data are shown to collapse reasonably well along rays emanating from the post-potential-core region of the jet. An application of the generalized Burgers equation is used to demonstrate the effect of cumulative nonlinear distortion on an arbitrary acoustic waveform produced by a high-convective-Mach-number supersonic jet. It is advocated that cumulative nonlinear distortion effects during far-field sound propagation are too subtle in this range-restricted environment and over the region covered, which may be true for other laboratory-scale jet noise facilities.

Key words: acoustics, aeroacoustics, jet noise

1. Introduction

Extensive theoretical, numerical and experimental studies have been conducted over the past four decades to understand the noise produced by supersonic jet flows. Unlike subsonic jets, the noise produced by supersonic jets can be categorized into four

† Present address: The University of Melbourne, Parkville VIC 3010, Australia.
Email address for correspondence: wbaars@unimelb.edu.au
‡ Present address: AdBm Technologies, Austin, TX 78702, USA.

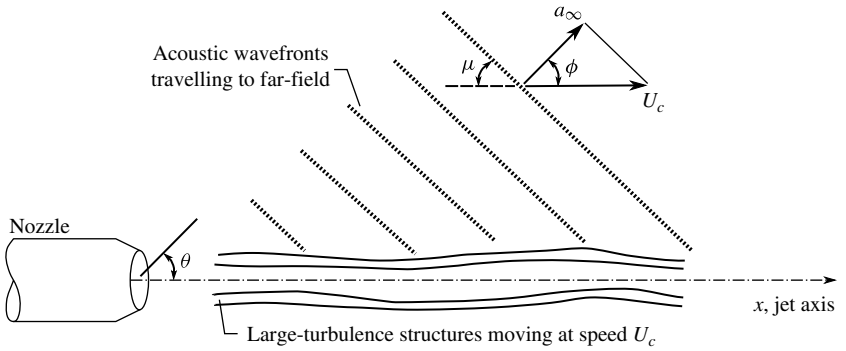

FIGURE 1. Simplified schematic of the Mach wave radiation mechanism in the near-field of the supersonic jet (ambient sound speed a_∞ and convective speed U_c of the instability waves).

distinct mechanisms (Tam 1995): turbulent mixing noise, broadband shock-associated noise, screech and transonic resonance. The latter three occur when shock structures are present. Restricting one's attention to turbulent mixing noise, the more relevant assemblage of literature reduces to the laboratory-scale jet studies of McLaughlin, Morrison & Troutt (1975), Tanna & Dean (1975), McLaughlin, Bridges & Kuo (2010), Papamoschou, Morris & McLaughlin (2010), Baars *et al.* (2011) and Kuo, Veltin & McLaughlin (2012), the full-scale flight tests of Morfey & Howell (1981) or the numerical studies of Morris (1977), Howell & Morfey (1987) and Seiner, Bhat & Ponton (1994). Aside from conventional spectral analysis, Laufer, Schlinker & Kaplan (1976), Gallagher & McLaughlin (1981), Petitjean, Viswanathan & McLaughlin (2006), Veltin, Day & McLaughlin (2011) and Baars & Tinney (2014) studied the temporal characteristics of the acoustic waveform in a laboratory environment while Gee *et al.* (2008) focused on sound produced by a full-scale static jet engine.

Like subsonic jets, the dominant sound produced by shock-free supersonic jets is caused by turbulent mixing noise (Viswanathan 2004). The formation and evolution of the large-scale structures associated with this mechanism encompasses various families of instability waves (Tam & Hu 1989). One particular family acts as surface panels convecting at supersonic speeds that radiate waves at the Mach cone half-angle: $\phi = \cos^{-1}(a_\infty/U_c)$, as is shown in figure 1. This pattern forms within the zone of action where acoustic radiation becomes increasingly intense as the convective acoustic Mach number of the large turbulent structures becomes supersonic. Analytical models describing the generation of Mach waves were developed by Phillips (1960) and Ffowcs Williams & Maidanik (1965); however few reliable experiments were available at that time to verify their accuracy. A decade later the noise produced by Mach waves became the subject of numerous investigations (McLaughlin *et al.* 1975; Laufer *et al.* 1976; Seiner *et al.* 1994; Tam & Chen 1994; Tam *et al.* 2008; Tam 2009). This is attributed to the fact that the noise produced by Mach waves is the dominant component of turbulent mixing noise and therefore researchers have attempted to tackle this component in order to achieve significant jet noise reduction (Papamoschou & Debiasi 1999).

Nonlinear distortion of acoustic waveforms is considered a prerequisite to understanding the process by which sound waves propagate from supersonic jets. However, there continues to be a lack of consensus as to how these sound waves

manifest nonlinearities. A common method for determining if nonlinearities are present in the waveform is to project the spectra acquired from a near far-field observer to a far far-field observer using a linear methodology and to compare the projected spectra to the actual measurement at that location (Viswanathan 2008). If spherical spreading and atmospheric absorption effects are properly accounted for then one is led to believe that the residuals between projected and measured waveforms are attributed to nonlinear distortion. This however requires that the propagation path be known, which is rarely the case in most laboratory and full-scale jet studies due to the expense of acquiring multiple observer locations.

Cumulative waveform distortions that become more pronounced with propagation distance are caused by points on the waveform possessing different amplitudes and propagating at different speeds (Hamilton & Blackstock 2008). Such distortions include waveform steepening, shock formation, shock coalescence and relaxation; the first of these shifts energy upward in the frequency spectrum. Stronger shocks that travel faster than weaker ones cause shocks to coalesce, thereby reducing the number of zero crossings; this is reflected by a shift of energy from mid frequencies to low frequencies. If viscous absorption permits, an overall broadening of the spectrum occurs.

Where model equations are concerned, nonlinear terms need to be retained in order for the acoustic waveform to distort. This can be seen in the seminal work of Pestorius & Blackstock (1974) which resulted in the development of a hybrid time-frequency algorithm that numerically solves the generalized Burgers equation for broadband signals. In particular, the algorithm is capable of propagating arbitrarily shaped waveforms in one dimension while incorporating shock formation and relaxation effects using nonlinear acoustic theory. The input waveform is propagated in a stepwise manner by first applying nonlinear distortion using the Earnshaw solution (Hamilton & Blackstock 2008). Absorption, dispersion, and geometrical spreading losses are accounted for in the frequency domain while the algorithm can be formulated to perform both linear and nonlinear predictions of the input waveform. While the use of the generalized Burgers equation to predict waveform steepening in plane waves and spherical waves has had considerable success (Pestorius & Blackstock 1974; Webster & Blackstock 1978; Hammerton & Crighton 1993), less favourable results have been encountered with problems concerning jet noise. Beginning with the pioneering work of Ffowcs Williams, Simson & Virchis (1975), the lack of cumulative waveform steepening in the pressure waveform was attributed to low amplitude levels at the source (personal communication between D. T. Blackstock and J. E. Ffowcs Williams). Only in recent years has a successful execution of this algorithm been performed on high-speed jets using full-scale tactical aircraft engines (Gee *et al.* 2008).

An alternative to the generalized Burgers equation algorithms can be found in the work of Howell & Morfey (1987) whereby a nonlinear indicator can be used to quantify how the energy in the power spectrum is redistributed due to nonlinear distortion; further details are discussed in § 5.2. A shortcoming of this indicator is that it requires one to compute the normalized quadrature spectral density, whose amplitude is highly sensitive to the shape of the signal's probability density function (p.d.f.). Likewise, many applications of this nonlinear indicator to problems in jet noise employed signals from only a single observer. This assumes that the statistical properties of the jet noise source is known, which continues to elude even the modern marvels of computational acoustics.

1.1. *Overview of the current study*

While a great number of surveys have focused on noise from supersonic jets, very few have attempted to investigate nonlinear acoustic phenomena in a spatial domain covering the acoustic near- and far-fields. The current study includes measurements in the acoustic field of a shock-free, unheated, Mach 3 jet. This high Mach number ensures the formation of Mach waves, which we believe can provide insightful information about how the sound propagates from lower-Mach-number jets. Moreover, due to the spatial range that is covered with these measurements, we can explicitly address relationships between local and cumulative nonlinear acoustic distortions.

Measurements comprise acoustic waveforms acquired on a grid in the (x, r)-plane of the jet, where x and r are axial and radial direction respectively. These are unique in the sense that sufficient spatial information is available in order to make valid conclusions regarding propagation trends. Spectral features of the sound field from this Mach 3 jet are described in § 3, followed by a discussion of the difficulties associated with studying cumulative nonlinear propagation in a laboratory-scale (range-restricted) environment in § 4. A scaling model is proposed that allows one to predict indicators of cumulative nonlinearities and the relationship between laboratory and full-scale experiments. It is inferred from this model that significant cumulative nonlinear distortions are absent from our acoustic data set. Evidence of this is shown in § 5 using time-averaged scalar metrics and an application of the Morfey–Howell indicator.

2. Experimental arrangement

2.1. *Facility*

Experiments were performed in a fully anechoic chamber and open jet wind tunnel located at the J. J. Pickle Research Campus of The University of Texas at Austin. A plan view of this facility is shown in figure 2. The anechoic chamber has interior dimensions of 5.8 m (L) × 4.6 m (W) × 3.7 m (H) (wedge tip to wedge tip) and provides 99 % normal incidence sound absorption for frequencies above 100 Hz. A modular jet rig is installed along the centreline of the wind tunnel and chamber as shown in figures 2 and 3(a,c). Further details on this facility are discussed by Baars & Tinney (2013).

The convergent–divergent nozzle was designed using the method of characteristics to have an exit gas dynamic Mach number of $M_e = 3.00$ (total temperature, $T_0 = 273.15$ K, ratio of specific heats, $\gamma = 1.4$, specific gas constant of air, $R = 287.05$ J kg^{-1} K^{-1}). The exit diameter was constrained to 25.4 mm resulting in a throat-to-exit length of 58.4 mm. All measurements were performed with the nozzle operating under perfectly expanded conditions with a mass flow of 1.04 kg s^{-1}.

2.2. *Instrumentation*

Acoustic data were acquired using four 1/4 in. prepolarized, pressure-field, condenser microphones (PCB model 377B10 capsules with model 426B03 preamplifiers). Microphone signals were digitized using a NI PXI-4472 card which provided the necessary IEPE power to operate the microphones all the while conditioning the input signal to eliminate aliasing prior to digitization (filter roll-off occurs at 0.84 times the Nyquist frequency). All four channels were acquired synchronously at a rate of 102.4 kS s^{-1} with 24 bit resolution for a minimum of 2^{20} samples. Microphone diaphragms were oriented at grazing incidence to the acoustic wave fronts (plane of the diaphragm intersecting the complete jet axis; see Viswanathan 2006) and with

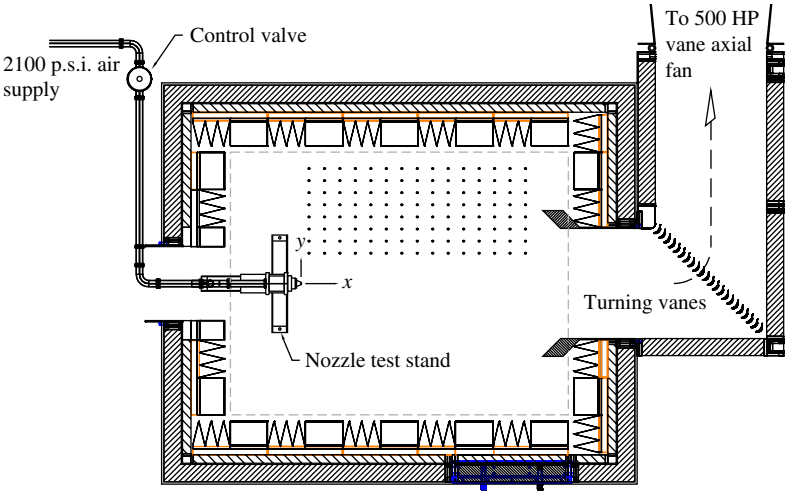

FIGURE 2. (Colour online) Plan view of the fully anechoic chamber and open jet wind tunnel at The University of Texas at Austin with the nozzle test rig installed (to scale). The microphone locations (projected on the (x, y)-plane) during the planar grid measurements are indicated by the dark circles.

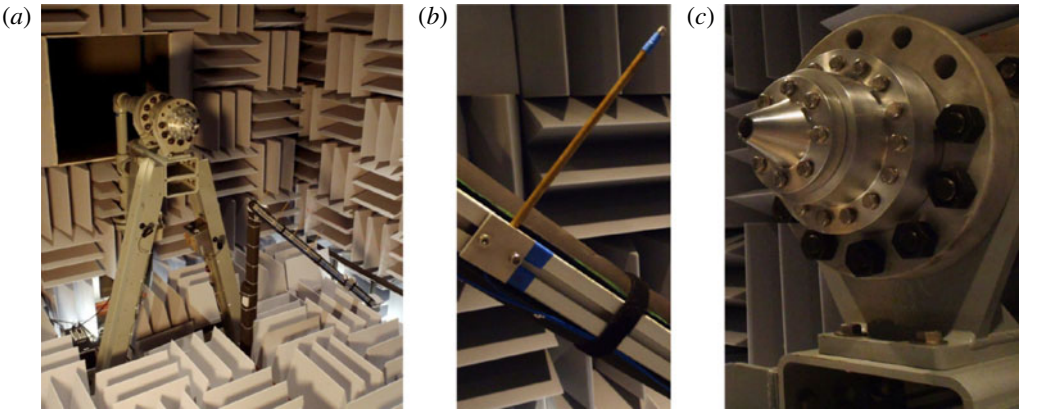

FIGURE 3. (Colour online) (*a*) Arrangement of the chamber during grid measurements. (*b*) Detail of the microphone support. (*c*) The Mach 3 MOC nozzle mounted on the ø6 in. settling chamber.

grid caps removed. Two different microphone configurations were used: a planar grid intersecting the jet axis (identified by dark circles in figure 2) and a line-array positioned along the Mach cone half-angle. Coordinates for the two configurations are provided in figure 4(*a*,*b*).

2.2.1. *Planar grid measurements*

The planar grid measurements were acquired on an (x, r)-plane oriented at an angle of $\varphi = -38.5°$. This uniform grid spanned from $5D_j$ to $145D_j$ in the axial direction and from $25D_j$ to $95D_j$ in the radial direction with a spacing of $\Delta x = \Delta r = 10D_j$, where D_j is jet exit diameter. The location of this grid encompasses the geometric

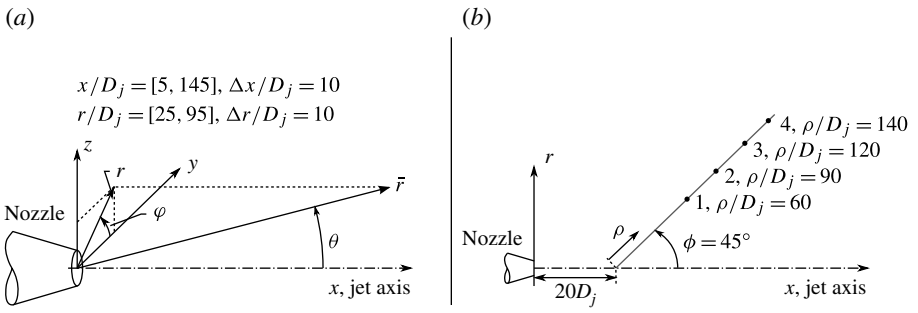

FIGURE 4. Coordinate system of the (*a*) planar grid and (*b*) four-microphone line-array measurements (in $\varphi = -38.5°$ plane).

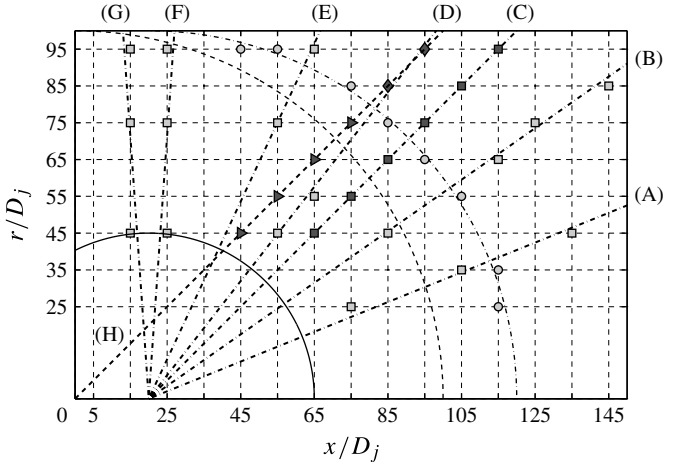

FIGURE 5. Microphone observer positions used to construct various line-arrays labelled A–H. Lines A–G (□) radiate from a point at $x/D_j = 20$; line H (△) radiates from the nozzle exit plane. An artificial arc-array (○) at $\rho/D_j = 100 \pm 1.5\,\%$ is centred on $x/D_j = 20$.

far-field where most jet noise measurements are performed. An acoustically transparent array was constructed that supported the four microphones using 12 in. long, 1/4 in. diameter tubes, as is shown in figure 3(*a*,*b*). The traversing array was repositioned in between runs to capture acoustic data at all grid positions.

In order to facilitate subsequent discussion, several grid points were selected in order to form both line- and arc-arrays of acoustic observers. Figure 5 provides a visual mapping of these observer points. The first of these comprised eight microphones forming an artificial arc-array at $\rho/D_j = 100 \pm 1.5\,\%$ and centred at $x/D_j = 20$. The precise locations of these eight acoustic observers are listed in table 1 and are further denoted by microphones 1–8. Several lines radiating from $x/D_j = 20$ were then formed, labelled A–G in figure 5. Subsequent discussions employ subscripts (increasing with outward radial distance) to indicate which microphone is being used. For example, microphone C_4 is located at $(x, r) = (95, 75)D_j$. Furthermore, lines A–G are angled at $\phi = [22,\ 35,\ 45,\ 52,\ 65,\ 86,\ 94]°$, respectively. A final line, H, also shown on figure 5, originates from the nozzle exit plane.

Mic. no.	1	2	3	4	5	6	7	8
$(x, r)/D_j$	(115, 25)	(115, 35)	(105, 55)	(95, 65)	(85, 75)	(75, 85)	(55, 95)	(45, 95)
ϕ (deg.)	14.7	20.2	32.9	40.9	49.1	57.1	69.8	75.3
ρ/D_j	98.2	101.2	101.2	99.3	99.3	101.2	101.2	98.3

TABLE 1. Microphone locations used to form an artificial arc-array centred at $x/D_j = 20$.

2.2.2. *Line-array measurements*

After the planar grid measurements were processed, the peak noise path was found to emanate from the post-potential-core region near $x/D_j = 20$, and along a path oriented at 45° from the jet axis. A line-array of four microphones was then positioned so as to follow this path. As can be seen from figure 4(*b*), all four microphones were positioned at one azimuth angle φ. The acoustic waveforms were not obstructed by upstream microphones due to their 1/4 in. tube supports (figure 3*b*).

2.3. *Test conditions*

Experiments were conducted over a duration of three days with weather conditions being monitored periodically throughout the study. A summary of these conditions is provided in table 2 using subscripts $j, \infty, 0$ to denote jet exit, ambient and stagnation conditions, respectively. Column 'grid-array (day 1)' corresponds to the measurements performed in the range $x/D_j = [5, 95]$, $r/D_j = [25, 95]$, whereas column 'grid-array (day 2)' pertains to the remaining section of the grid: $x/D_j = [105, 145]$, $r/D_j = [25, 95]$. Jet exit conditions were calculated from standard isentropic relations using an estimate for the dynamic viscosity based on Sutherland's law.

A useful metric for predicting the formation of Mach waves in a jet is known as the Oertel convective Mach number, defined as $M_{co} = (U_j + 0.5a_j)/(a_j + a_\infty)$. If $M_{co} < 0.75$ then Mach waves are non-existent, for $0.75 < M_{co} < 1$ the Mach waves are in their developing stages, and for $M_{co} > 1$, Mach waves are expected to be fully developed. For our jet, $M_{co} = 1.31$, which suggests that these conditions are more than adequate for generating strong Mach waves.

2.3.1. *Convective velocity*

The convective speed of the large-scale turbulent structures is a prerequisite for calculating the Mach wave radiation angle. Here we have chosen to assume $U_c = 0.8U_j$, which was motivated by the findings of McLaughlin *et al.* (1975) and Troutt & McLaughlin (1982) who showed phase velocities of the axial instability waves to be of this magnitude over a broad range of wavenumbers; similar findings were reported by Kerhervé, Fitzpatrick & Jordan (2006). A recent study by Tinney, Ukeiley & Glauser (2008), based on near-field pressure and velocity correlations, has also shown how low-mode-number disturbances, residing on the high-speed sides of the annular shear layer, convect at speeds near $0.8U_j$. These low-mode-number events correlate well with the far-field pressure (Hall *et al.* 2009). Norum & Seiner (1982) on the other hand, achieved reasonable results using $0.7U_j$.

3. Basic acoustic-field observations

3.1. *Statistics*

The topography of the overall sound pressure level (OASPL) obtained from the planar grid measurements is presented in figure 6. Experimentally acquired contours can also

		Grid-array (day 1)	Grid-array (day 2)	Line-array (day 3)
	M_j		$3.00 \pm 1\,\%$	
	$NPR = p_0/p_\infty$		$36.73 \pm 4.5\,\%$	
Measured	p_∞ (kPa)	100.7	100.8	101.2
	T_0 (K)	291.2	286.2	285.1
	T_∞ (K)	293.3	287.2	287.5
	RH (%)	75.4	63.2	48.2
Calculated	T_j (K)	104.0	102.2	101.8
	a_j (m s^{-1})	204.4	202.7	202.3
	a_∞ (m s^{-1})	343.3	339.7	339.9
	U_j (m s^{-1})	613.3	608.0	606.9
	$f_c = U_j/D_j$ (kHz)	24.1	23.9	23.9
	T_j/T_∞	0.35	0.36	0.35
	ρ_∞/ρ_j	0.35	0.36	0.35
	Re_j	7.4×10^6	7.6×10^6	7.6×10^6
	$U_c = 0.8U_j$ (m s^{-1})	490.6	486.4	485.5
	$M_a = U_j/a_\infty$	1.79	1.79	1.79
	$M_c = U_c/a_\infty$	1.43	1.43	1.43
	ϕ (deg.)	45.6	45.7	45.6

TABLE 2. Summary of experimental conditions for the microphone grid-array and line-array measurements (M_j was controlled to be the fully expanded Mach number $M_e = 3.00$).

be found in the literature (Potter & Crocker 1966; McLaughlin *et al.* 1975; Gallagher & McLaughlin 1981; Varnier 2001; Greska *et al.* 2008). The classical heart-shaped pattern and cone of silence are observed. A strong intensity gradient centred along $\theta = 45°$ (initiating from the jet exit) is also observed and supports the notion that Mach wave radiation intensity decays rapidly beyond the Mach wave angle. Furthermore, the edge remains distinct with outward distance up to, and probably beyond, the range of consideration.

The acoustic pressure decay along the peak noise emission path is presented in figure 7. Experimental data from both grid- and line-array measurements are corrected for atmospheric absorption. A linear spherical decay trend is matched to the grid-array measurements in a minimum root-mean-square-error sense. Subsequently, the pressure decay associated with cylindrical spreading is indicated for reference. It is observed that the experiment closely resembles the spherical decay. And so, for subsequent analyses, it is assumed that the sound propagates along a path coinciding with the peak OASPL and that its amplitude obeys a spherical decay law.

3.1.1. *Core lengths of the jet*

No centreline data are available for the current study, and so empirical formulations are used to determine the potential core length ($L_c = x_c/D_j$) and the length of the supersonic region ($L_s = x_s/D_j$). Nagamatsu & Horvay (1970) showed that $L_c = 5.22M_j^{0.90} + 0.22$ and $L_s = 5M_j^{1.8} + 0.8$ worked well for a broad set of conditions and that the location of most intense sound generation ($L_p = x_p/D_j$) resided just upstream of the sonic point in the so-called transition region, but always downstream of the potential core: $L_c < L_p < L_s$. These observations were similar to the findings

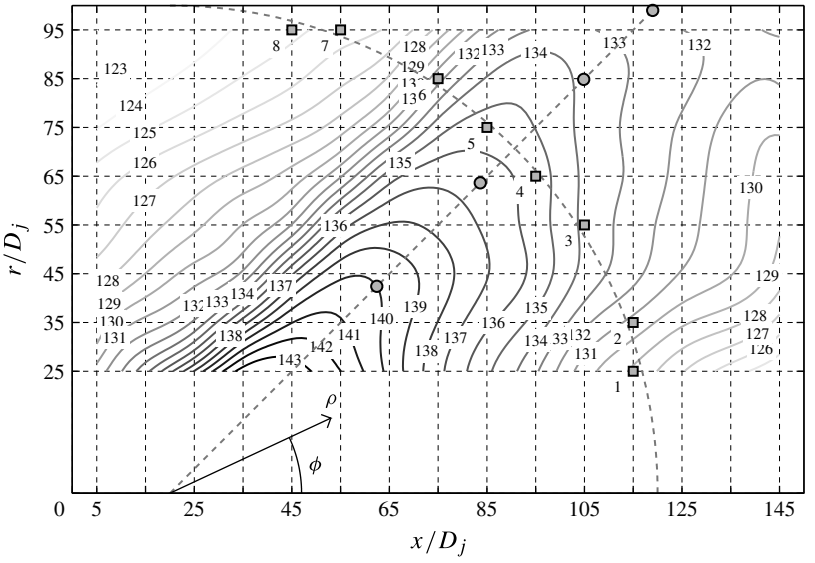

FIGURE 6. Contours of OASPL in dB, $p_{ref} = 20$ μPa, taken from Baars & Tinney (2014). Data of the original grid ($10D_j$ spacing) are interpolated by a factor of 10. Superposed are the grid points forming the artificial arc-array, and the line-array measurement locations are also indicated.

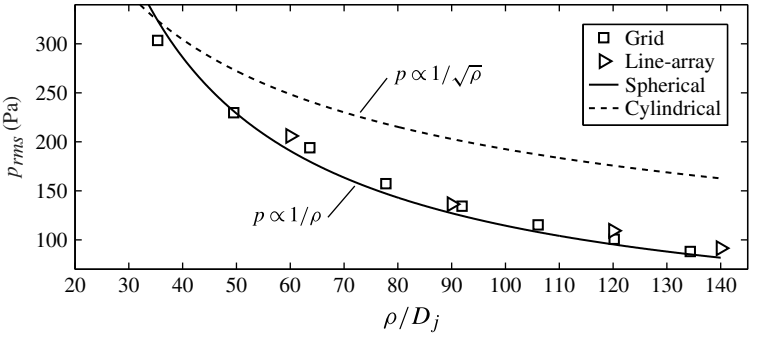

FIGURE 7. Decay of the pressure standard deviation along the peak noise path ($\phi = 45°$).

of Potter (1968). Varnier (2001) later concluded that the estimate of Nagamatsu & Horvay (1970) for L_s was adequate in describing the most pronounced sound source location. However, Varnier (2001) found that for a slightly overexpanded jet, $M_j = 2.8$ ($M_e = 3.3$, M_e being the design Mach number), L_p resided further upstream at $L_s/L_p \approx M_j^{\alpha}$ with $\alpha = 0.85$, and that the potential core length was estimated by $L_s/L_c \approx M_e^{0.9}$. Surprisingly, the jet temperature does not appear explicitly in the previous formulations. In an effort to overcome this deficiency, Greska *et al.* (2008) suggested that $L_c = 3.134 \exp(1.043M_j - M_c)$; the convective Mach number is affected by differences in temperature between the core and ambient gases. Lastly, the model proposed by Witze (1974) is considered here, which governs only supersonic unheated jets.

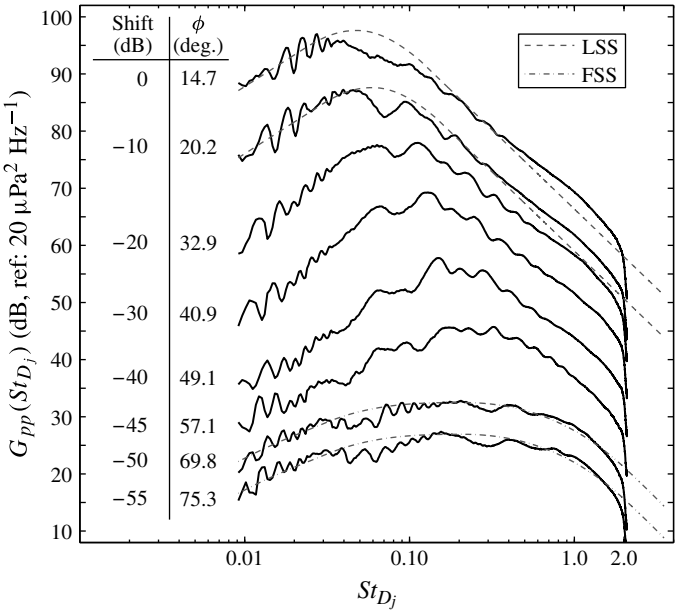

FIGURE 8. PSDs along the artificial arc-array (5 % bandwidth moving filter). Spectra at shallow and side-line angles are compared to large-scale similarity (LSS) and fine-scale similarity (FSS) trends, respectively.

Model	L_c	L_p	L_s
Nagamatsu & Horvay (1970)	14.3	—	36.9
Varnier (2001)	13.7	14.5	36.9
Greska *et al.* (2008)	17.1	—	—
Witze (1974)	18.3	—	—
Current experimental data	—	17.5	—

TABLE 3. Potential core length, location of most intense noise production, and length of the supersonic region for the Mach 3 jet according to various models.

A summary of the results obtained from these aforementioned models is provided in table 3. An estimate for the location of maximum peak pressure fluctuations, obtained by way of linear extrapolation of the peak OASPL, has also been included for comparison. Visual inspection of figure 6 suggests that $L_p = 17.5D_j$ is reasonable, and so it will be used throughout the remainder of the analysis.

3.2. *Spectral distribution of sound*

Estimates of the one-sided power spectral densities (PSDs) from points located on the artificial arc-array (table 1) are presented in figure 8 using a frequency resolution of $\delta f = 12.2$ Hz (or in terms of Strouhal number, defined as $St_{D_j} = fD_j/U_j$, $\Delta St_{D_j} = 5.1 \times 10^{-4}$) and $N = 8192$ samples per bin. Low-frequency wiggles ($St_{D_j} < 0.03$) are attributed to facility reflections based on the first fundamental frequencies identified in the spectra and the distance from each observer position to the chamber wall.

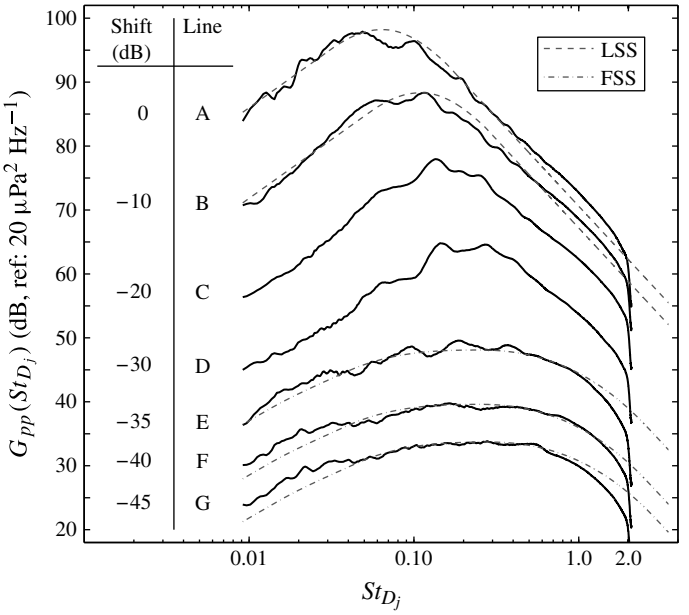

FIGURE 9. PSDs along spreading lines A–G (5 % bandwidth moving filter). Spectra are averaged from the microphones along the lines after being linearly scaled to $\rho/D_j = 100$.

Additional spectra are presented in figure 9 and are computed by first scaling each point to $\rho/D_j = 100$ and then averaging points that share the same polar position for a given spreading line (A–G). The scaling involves a simple linear spreading concept with corrections for humidity. An illustration of this process is shown in figure 10(*a*) for microphone observers located along line C and are shown to overlay one another quite well. Wiggles in the spectra at $\rho/D_j = 140$ are observed and are believed to be caused by changes in the flow resistive properties of the melamine foam (that the acoustic wedges are constructed from) due to rather high relative humidity levels in the chamber (63 %–75 %) during the first two days of testing. Proof of this is shown in figure 10(*b*) by comparing the pressure spectra at two microphone locations and under different relative humidities (RH); the general features are unaffected.

Nevertheless, spectra in figures 8, 9 and 10(*a*,*b*) display two well-accepted trends that are typical of supersonic jet noise: that is, a pronounced ridge at shallow angles ($\phi \lesssim 49.1°$) indicative of the noise produced by Mach wave radiation, and broadband lower-amplitude spectra at sideline angles ($\phi \gtrsim 57.1°$) typical of the fine-scale turbulence mixing noise. Large-scale similarity (LSS) and fine-scale similarity (FSS) spectra (Tam, Golebiowski & Seiner 1996; Tam *et al.* 2008) have been included and demonstrate good agreement for the shallow and sideline angle observers, respectively.

Contours of sound pressure intensity at various Strouhal numbers are illustrated in figure 11(*a–f*). This is obtained by applying a band-pass filter that averages over 20 % of the chosen centre frequency. Figure 11(*a*,*b*) reveals peak intensities of the low frequencies radiating at angles shallower than the Mach wave radiation angle with lines emanating from an origin located downstream of the post-potential core ($x \gtrsim 17.5D_j$). This is caused by a considerable drop in axial phase velocity of the instability waves for low frequencies ($St < 0.2$) (Troutt & McLaughlin 1982). For frequencies centred around $St_{D_j} = 0.2$ in figure 11(*c*), the peak radiation angle

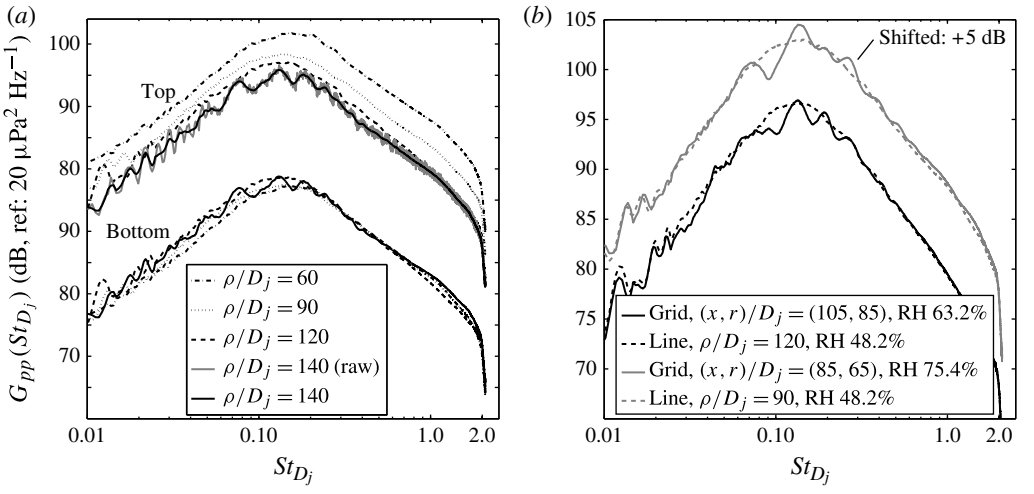

FIGURE 10. (*a*) PSDs along the line-array (5 % bandwidth moving filter): unscaled spectra (top), spectra linearly scaled to $\rho/D_j = 100$ (bottom). (*b*) Effect of relative humidity on the pressure spectra at two microphone locations along the line-array.

follows along the Mach wave radiation angle. Spectra that are filtered around higher centre frequencies (figure 11*d–f*) appear to have origins that are shifted upstream, but never originate from the nozzle exit plane. These findings are in agreement with Kuo, Veltin & McLaughlin (2010) who observed that the angular orientation of the lobe of peak intensity remained mostly unchanged with frequency for an unheated Mach 1.5 jet. Contrary to the current result, Kuo *et al.* (2010) observed a broadening of the lobe at higher frequencies and concluded that this was more consistent with the notion that the noise pattern produced by the fine-scale turbulence was more omni-directional. Here, a broadening is not explicitly observed. A plausible explanation for this discrepancy is the high convective Mach number in this study. Hence, the highly directional Mach wave radiation process saturates more of the higher-frequency omni-directional noise content. In general, these findings support the notion that high-frequency noise radiates from regions close to the nozzle exit, while low-frequency noise dominates locations further downstream.

4. Acoustic nonlinearities from a laboratory-scale jet

Numerous efforts have been undertaken to investigate nonlinear sound propagation from jet flows. Crighton & Bashforth (1980) and Crighton (1986) have developed analytical models to investigate changes in jet noise propagation due to nonlinear phenomena. Experimental studies in range-restricted environments include the work of Gallagher & McLaughlin (1981) and Petitjean *et al.* (2006). Only weak cumulative nonlinear effects have been observed using a laboratory-scale setup, while strong nonlinear effects have been observed under full-scale conditions. Examples of full-scale jet and rocket tests can be found in the literature (Morfey & Howell 1981; McInerny 1996; McInerny & Ölçmen 2005; Gee *et al.* 2008; Saxena, Morris & Viswanathan 2009). Here, a scaling model is introduced that could be used to guide future studies aimed at predicting whether acoustic waveforms produced by jet flows will undergo cumulative nonlinear distortion.

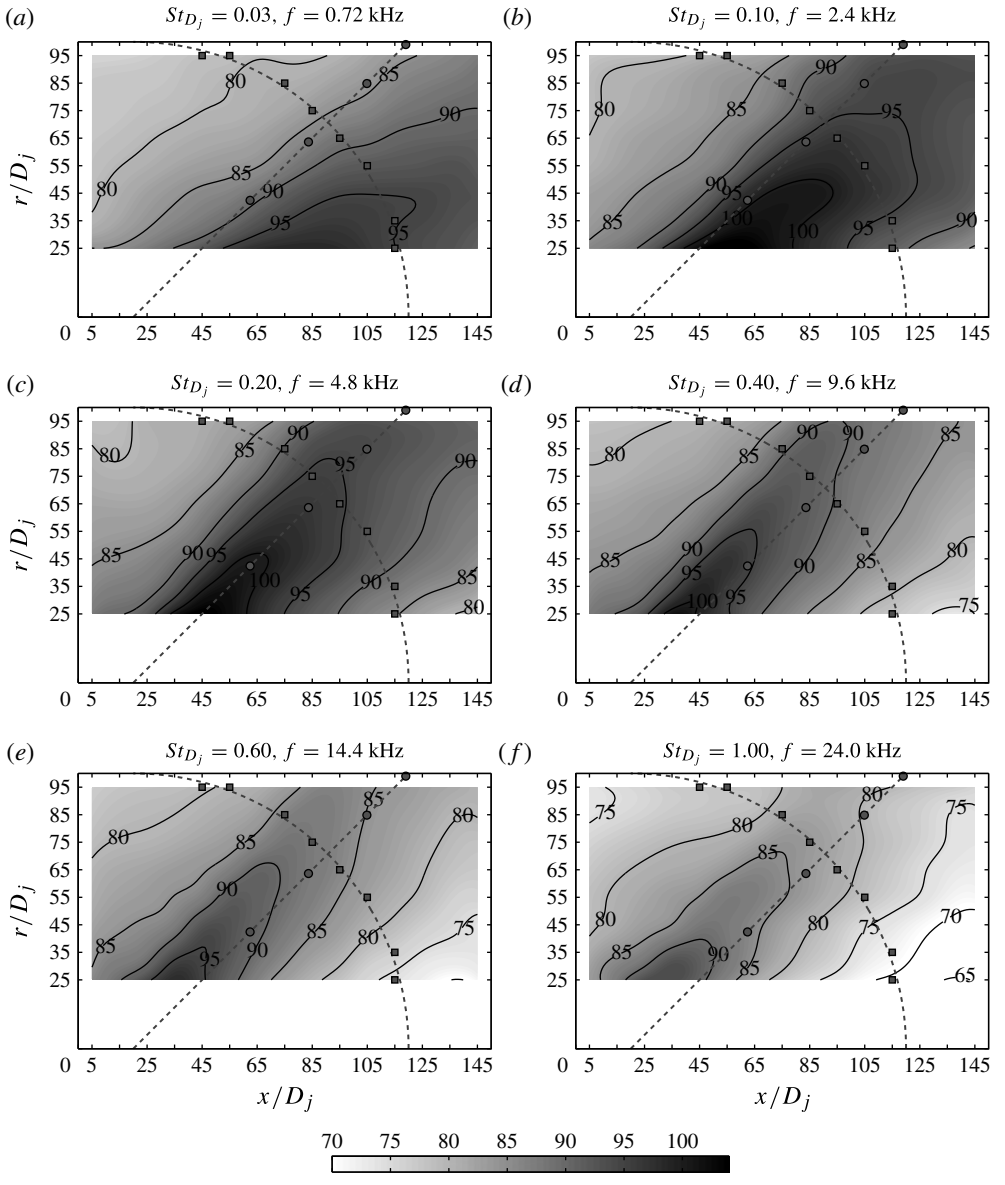

FIGURE 11. Contours of the sound pressure level (SPL) in dB, ref: 20 μPa^2 Hz^{-1}. The SPL value is averaged over a domain spanning $\pm 20\,\%$ around the centre Strouhal number.

4.1. *Acoustic length scales*

A first step in determining if nonlinear distortion will occur is to consider two important acoustic length scales. The first of these is taken as the acoustic absorption length (l_a), which is the reciprocal of the absorption coefficient

$$l_a = \frac{1}{\alpha}. \tag{4.1}$$

For our laboratory conditions, the curves for the absorption coefficient for different RH are shown in figure 12(*a*) and are taken from appendix B of Blackstock (2000).

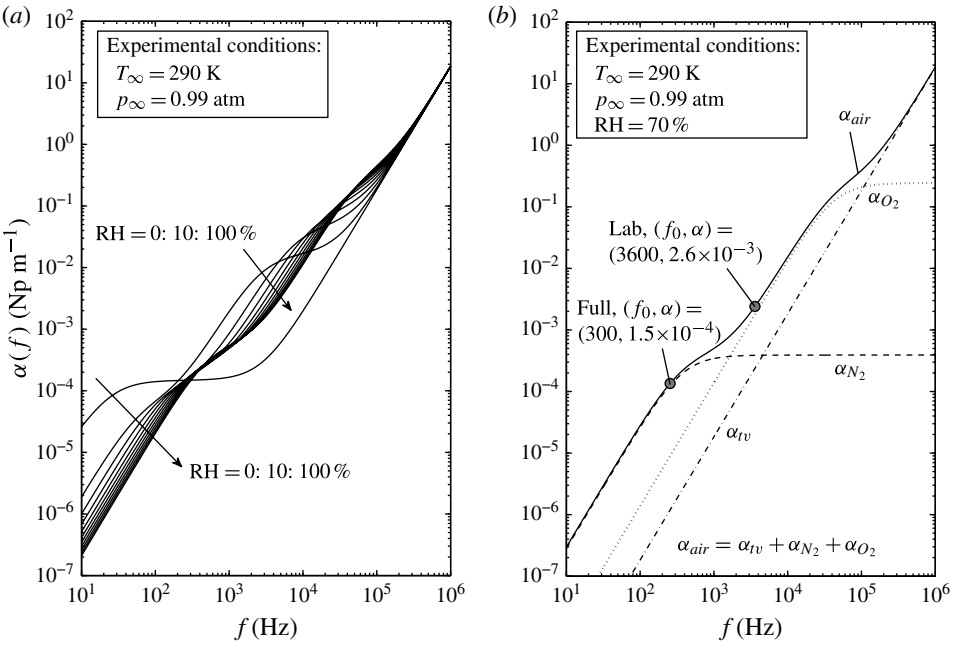

FIGURE 12. (*a*) Absorption curves for different RH taken from appendix B of Blackstock (2000). (*b*) The absorption curve for the experimental conditions during the acquisition of the grid measurements.

The coefficient has units of nepers per unit distance and can be converted to decibels per unit distance $\overline{\alpha}$ according to $\overline{\alpha}(f) = 8.686\alpha(f)$. Figure 12(*b*) presents the absorption coefficient for a relative humidity of 70 % (average humidity for our grid measurements) and demonstrates the various contributions from relaxation and thermoviscous absorption. Relaxation dominates at low frequencies and for air, two relaxation processes are involved: absorption associated with the vibration of both nitrogen molecules (α_{N_2}) and oxygen molecules (α_{O_2}). Thermoviscous effects (α_{tv}) dominate at higher frequencies and are expressed by the asymptotic formula

$$\alpha_{tv} = \frac{\delta\,(2\pi f)^2}{2a_\infty^3}, \tag{4.2}$$

where δ is the diffusivity of sound and has value 3.64×10^{-5} m^2 s^{-1}.

The second acoustic length scale is taken as the shock formation distance. For progressive plane waves with Gaussian waveform statistics (non-steepened) that are emitted by a broadband source, the shock formation distance, as introduced by Gurbatov & Rudenko (p. 383, Hamilton & Blackstock 2008), is

$$\overline{x} = \frac{\rho_\infty a_\infty^3}{\beta(2\pi f_0)p_{rms}}. \tag{4.3}$$

In (4.3), the ambient density is taken as $\rho_\infty = 1.223$ kg m^{-3}, the coefficient of nonlinearity is given by $\beta = (\gamma + 1)/2 = 1.2$, p_{rms} is the pressure standard deviation of the source, and f_0 is the centre frequency of the broadband source. Since the source field of a jet is complex, and mostly unknown, our analysis is confined to a

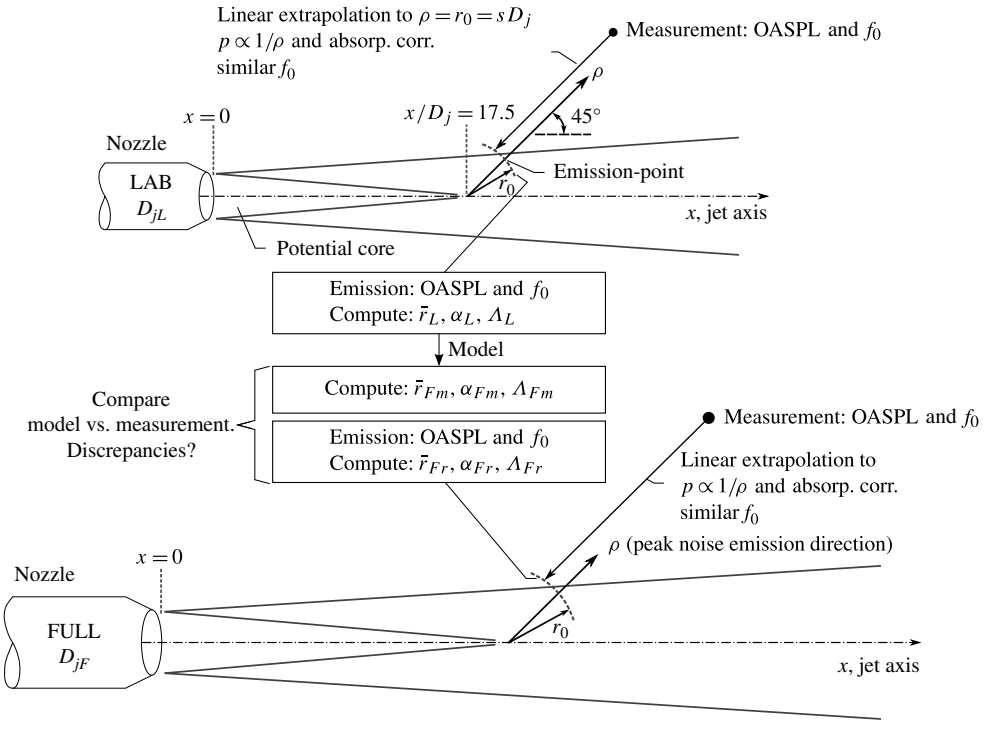

FIGURE 13. Concept of scaling approach indicating the comparison of characteristic nonlinear parameters between the model prediction (subscript *Fm*, '*m*' from model) and a full-scale measurement (subscript *Fr*, '*r*' from reference).

single sound ray propagating into the acoustic far-field. The ray is aligned with the peak noise angle and emanates from a point in the shear layer. This is reasonable since the most interesting region concerning nonlinear noise propagation resides along this ray. The location of this emission point scales with nozzle diameter, and is identified in figure 13 by $r_0 = sD_j$. For simplicity, the sound intensity is assumed to obey a spherical decay law (figure 7) along the peak noise angle. Therefore, only the spherical shock formation distance is considered and is denoted by $\bar{r}$ (Hamilton & Blackstock 2008) such that,

$$\bar{r} = r_0 \exp(\bar{x}/r_0)\,. \tag{4.4}$$

Shock formation distances are typically much larger for spherically spreading sound waves than for plane waves due to the spreading losses in the former that cause a more rapid decay in the waveform amplitude with distance and hence, a reduction of the steepening process.

As a next step, the pressure standard deviation (p_{rms}) and centre frequency (f_0) at the emission point are obtained by examining the measurements of the SPL presented in figure 10(*a*,*b*). The closest measurement along the peak noise direction ($\rho/D_j = 60$: OASPL = 140.1 dB and $f_0 = 3.6$ kHz) is extrapolated towards the emission point with corrections for atmospheric absorption; this assumes spherical spreading (figure 13). The initial amplitude of the sound ray at the emission-point is computed as $p_{rms} = 4948$ Pa (167.9 dB) and the centre frequency is assumed to

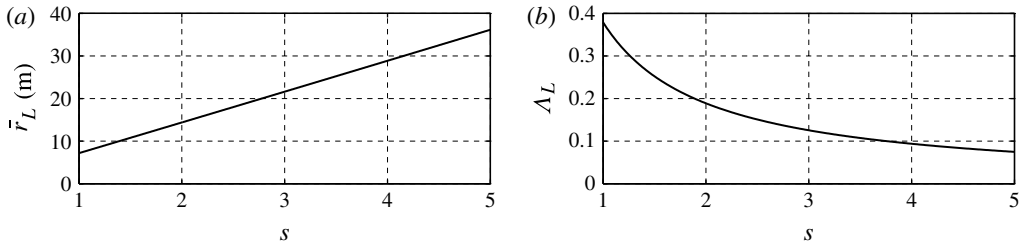

FIGURE 14. (*a*) Spherical shock formation distance and (*b*) effective Gol'dberg number for the laboratory-scale scenario as function of emission-point location $r_0 = sD_j$.

be equal to $f_0 = 3.6$ kHz. Using the aforementioned approach and parameters, the shock formation distance ($\bar{r}_L$), as function of scale s of the radial emission point, is presented in figure 14(*a*) where the subscript L refers to laboratory-scale conditions. The increasing trend is expected, since an emission point that is located further from the jet centreline is associated with a lower starting waveform amplitude, which causes the waveform to steepen less fast and thus extends the shock formation distance. Lastly, for the given centre frequency, the attenuation coefficient is found to be $\alpha_L = 2.60 \times 10^{-3}$ Np m^{-1} (indicated in figure 12*b*) which corresponds to an absorption length of $l_{aL} \approx 385$ m.

4.2. *Effective Gol'dberg number*

Having reviewed the two acoustic length scales of interest in this study (absorption length and shock formation distance), and the means by which they can be obtained from laboratory measurements, a parameter that is relevant to the occurrence of cumulative nonlinear distortion in the waveform is examined next. We will first review this parameter for the case of plane waves. Propagation of plane waves can be modelled by the following generalized form of the Burgers equation:

$$\frac{\partial p}{\partial x} = \frac{\beta p}{\rho_0 a_\infty^3}\frac{\partial p}{\partial \tau} + \psi_\tau \{p\}\,, \tag{4.5}$$

where p is acoustic pressure, x is the coordinate along the propagation path, ρ_0 is ambient density, $\tau = t - x/a_\infty$ is retarded time, and ψ_τ is the atmospheric absorption and dispersion operator. For a thermoviscous fluid, a non-dimensional form of (4.5) can be written as

$$\frac{\partial P}{\partial \sigma} = P\frac{\partial P}{\partial \theta} + \frac{1}{\Gamma}\frac{\partial^2 P}{\partial \theta^2}, \tag{4.6}$$

where $P = p/p_{rms}$, $\sigma = x/\bar{x}$ and $\theta = 2\pi f_0 \tau$ (Hamilton & Blackstock 2008, p. 312). Parameter Γ is the only adjustable coefficient in (4.6) and represents the importance of the viscosity term relative to the nonlinear term, since

$$\Gamma = \frac{1}{\alpha \bar{x}} = \frac{l_a}{\bar{x}}. \tag{4.7}$$

In the literature, Γ is known as the Gol'dberg number. Since this dimensionless number is equal to the ratio of the absorption length to the plane wave shock formation distance, it is therefore a measure of the strength of nonlinear distortion

relative to that of dissipation (Hamilton & Blackstock 2008). When $\Gamma \lesssim 1$, attenuation dominates and the formation of shocks is suppressed. When $\Gamma \gg 1$, cumulative nonlinear distortion is expected to occur. And so, for the case of plane waves, this single ratio of length scales is sufficient to determine whether significant cumulative nonlinear distortions arise in the waveform. Because the source signal in this work is broadband, the Gol'dberg number is dependent on the frequency that is selected. For simplification, the centre frequency (f_0) is selected for our analysis, as was done in computing the shock formation distance earlier; this is now denoted as the characteristic Gol'dberg number.

We turn our attention now to a spherical wave field. The generalized Burgers equation for spherically spreading waves may be expressed in dimensionless form as (Naugol'nykh, Soluyan & Khokhlov (1963); see also Hamilton & Blackstock 2008, p. 323)

$$\frac{\partial Q}{\partial \zeta} = Q\frac{\partial Q}{\partial \theta} + \frac{\exp(\zeta/\sigma_0)}{\Gamma}\frac{\partial^2 Q}{\partial \theta^2}. \tag{4.8}$$

Here, $\sigma_0 = r_0/\bar{x}$ is the ratio of source radius r_0 to the plane wave shock formation distance, $Q = (\sigma/\sigma_0)P$ is dimensionless pressure with spherical spreading removed, and $\zeta = \sigma_0 \ln(\sigma/\sigma_0)$ is a stretched coordinate. While the evolution of a plane wave is governed completely by the single dimensionless parameter Γ, two dimensionless parameters – length scale ratios Γ and σ_0 – determine how spherical waves evolve. It has been recently shown by Hamilton (2013) that an effective Gol'dberg number for diverging spherical waves may be expressed as

$$\Lambda = \Gamma \exp(-\zeta_{sh}/\sigma_0), \tag{4.9}$$

and $\zeta_{sh} = \pi/2$. Substitution of (4.9) in (4.8) results in the following form of the Burgers equation for spherical waves:

$$\frac{\partial Q}{\partial \zeta} = Q\frac{\partial Q}{\partial \theta} + \frac{\exp[(\zeta - \zeta_{sh})/\sigma_0]}{\Lambda}\frac{\partial^2 Q}{\partial \theta^2}. \tag{4.10}$$

Note that for $\Lambda \gg 1$ and in the neighbourhood of where shock formation occurs for an initially sinusoidal wave in the absence of losses (i.e. at $\zeta = 1$), the second term on the right-hand side, which accounts for losses, is negligible in comparison with the first term, which accounts for nonlinearity. As a result, shock formation is guaranteed for $\Lambda \gg 1$, whereas nonlinear effects are negligible for $\Lambda \lesssim 1$.

The effective Gol'dberg number Λ for the current laboratory-scale Mach 3 jet is shown in figure 14(*b*). For the entire range of emission-point locations considered, $\Lambda_L < 0.4$. A typical source size is estimated to span the width of the shear layer in the post-potential-core region of the flow. Given the relatively linear growth of the jet shear layer (roughly $0.10x$; see Tinney *et al.* 2008), an emission-point location scale of $s = r_0/D_j = 2.5$ is expected and is assumed to hold over a range of jet conditions. The resultant shock formation distance and effective Gol'dberg number for this laboratory-scale study are determined to be $\bar{r}_L(s=2.5) = 18.0$ m and $\Lambda_L(s=2.5) = 0.15$.

For typical full-scale conditions, where higher temperature ratios and larger nozzle diameters are anticipated, the centre frequency, and thus $\alpha(f)$, decreases. It will be shown below that under these conditions, $\bar{x}/r_0$ will decrease by a factor of about 14.2. Thus, the effective Gol'dberg number Λ will become larger in the full-scale study thereby making cumulative nonlinear effects more dominant in the matching full-scale

case. It is important to point out that (4.4) assumes that the emitted signal at $\rho = r_0$ possesses Gaussian statistics. It is shown later that the waveform distribution from the nearest far-field observer point is well-approximated with Gaussian statistics, but has sawtooth-like structures. And so, it is unclear whether the waveform is born in this way or has undergone a significant steepening process within the hydrodynamic periphery of the jet flow. Concurrent studies by Fiévet *et al.* (2013) suggest that waveforms are initially steepened at the source, but such measurements, when taken too close to the jet flow, become corrupted by hydrodynamic effects and the true form of the acoustic waveform is difficult to obtain. Nevertheless, the shock formation distance and Gol'dberg number are expected to decrease and increase, respectively, with pre-steepened waveforms, which will differ slightly from what is predicted by this model. This warrants additional analysis to determine what effect a pre-steepened wave has on the shock formation distance.

4.3. *Scaling the shock formation distance*

Scaling laws are derived for the occurrence of cumulative nonlinear waveform distortions between the laboratory- and full-scale environments in terms of jet exit parameters (i.e. D_j, M_j, T_j). First, the shock formation distance, (4.3) and (4.4), is scaled based on lossless fluid theory; this is the most favourable scenario for studying nonlinear effects, since the distance to shock formation is now the shortest possible ($\Lambda \to \infty$). In reality, absorption will delay, and partly suppress, this process. The physical meaning of this scaling will therefore be commented on later when the Gol'dberg number is scaled. Foremost, it is assumed that the propagation medium for the laboratory- and full-scale environments is the same (i.e. ambient air). On the other hand, it is not assumed in our formulations that the Strouhal number (St_{D_j}) corresponding to the peak SPL in the two environments is the same (variations in non-dimensional frequencies appear from changes in jet exit conditions, M_j and T_j). And so, peak frequencies are related by $f \propto St_{D_j} U_j / D_j$. Lastly, the sound intensity I for shock-free supersonic jets has been shown to vary with the jet exit velocity to the eighth power, thus $I \propto U_j^8$ (Lighthill 1954). Since the intensity is given by $I = p_{rms}^2/(\rho_\infty a_\infty)$, it can be shown that the emitted waveform amplitude satisfies $p_{rms} \propto U_j^4$. It has been further shown by Viswanathan (2004) that for a range of temperature ratios, the acoustic intensity still scales closely with U_j^8 for acoustic Mach numbers ranging from about 0.5 to 1.7. Upon inserting the aforementioned assumptions into (4.3), the following relationship unfolds:

$$\overline{x} \propto \frac{D_j}{U_j^5 St_{D_j}}. \tag{4.11}$$

In the most general case for a supersonic jet, and by repeatedly taking into account the equal-medium assumption, (4.11) can be written as

$$\overline{x} \propto \frac{D_j}{M_j^5 T_j^{2.5} St_{D_j}}. \tag{4.12}$$

Knowing that $r_0 = sD_j$, the exponent in (4.4) can be expressed as follows:

$$\frac{\overline{x}}{r_0} \propto \frac{1}{M_j^5 T_j^{2.5} St_{D_j}}, \tag{4.13}$$

which employs all of the jet parameters of interest. The shock formation distance between the laboratory-scale (denoted by L) and full-scale (denoted by F) environments can be related as follows:

$$\frac{\bar{r}_L}{r_{0L}} = \left(\frac{\bar{r}_F}{r_{0F}}\right)^{\eta}, \tag{4.14}$$

where the parameter η is obtained by substituting (4.13) into (4.4) and is defined as

$$\eta = \eta\left(M_j, T_j, St_{D_j}\right) = \frac{\bar{x}_L/r_{0L}}{\bar{x}_F/r_{0F}} = \left(\frac{M_{jF}}{M_{jL}}\right)^{5}\left(\frac{T_{jF}}{T_{jL}}\right)^{2.5}\left(\frac{St_{D_{jF}}}{St_{D_{jL}}}\right). \tag{4.15}$$

Because geometric scaling is observed throughout the literature, one may prefer to normalize the shock formation distance (4.14) by the nozzle exit diameter, which results in the following expression:

$$\frac{\bar{r}_L}{D_{jL}} = \left(\frac{\bar{r}_F}{D_{jF}}\right)^{\eta} s^{(1-\eta)}. \tag{4.16}$$

Here we show how (4.16), in combination with (4.15), constitutes a reasonable scaling relationship for the shock formation distance in terms of jet exit parameters.

In an effort to illustrate the scaling laws, we will first consider variations in η under different laboratory-scale conditions. This requires a full-scale reference case to be selected from the literature; we will resort to a recent study by Gee *et al.* (2012). Their study comprised surveys of the far-field acoustics from a Pratt & Whitney F-135 engine installed in an F-35A military aircraft. The exit conditions of this study were approximated to be $M_{jF} = 1.4$ and $T_{jF} = 1000$ K (the engine was operated at military, 100 % ETR, power) with a nozzle exit diameter of $D_{jF} = 0.95$ m. It was found that the foregoing assumptions of the jet operating conditions had little influence on the results. Gee *et al.* (2012) observed peak OASPLs of 138.8 dB at a radial location of $\rho/D_{jF} = 80$ (centred 6.7 m aft of the aircraft) and at an angle of 50° from the jet axis. The centre frequency along the peak direction was found to be 300 Hz and tests were conducted with relative humidity levels of 24 % ($\alpha_F = 1.48 \times 10^{-4}$ Np m^{-1}). This full-scale reference case is used throughout the remainder of this section. Given the full-scale conditions of Gee *et al.* (2012), the parameter η is determined from (4.15) and found to be 14.2 (see point 1 in figure 15). We will show later on how a reasonable prediction of the Gol'dberg number pertaining to the full-scale conditions can be determined from any laboratory-scale tests.

Variations in η are illustrated in figure 15 for a wide range of operating conditions ($1.0 < M_{jL} < 3.5$ and 50 K $< T_{jL} <$ 1200 K). It is important to note that in this visual representation, Strouhal number remains constant at $St_{D_{jL}} = 0.15$ for the laboratory-scale case (based on our operating conditions) and at $St_{D_{jF}} = 0.32$ for the full-scale case. The correct mapping of $St_{D_{jL}} = St_{D_{jL}}(M_{jL}, T_{jL})$ is currently unknown. However, $St_{D_{jF}}/St_{D_{jL}} = 1$ if temperature and Mach numbers are matched, and so η should equal one under such conditions. And so, since the effect of Strouhal ratio on η is not accurately accounted for under varying jet conditions (differences in Mach number and temperature ratios between laboratory- and full-scale), figure 15 is, strictly speaking, only valid for point 1 from our current study. However, the magnitude of η does not change significantly (remains within the same order of magnitude) when different laboratory-scale studies are considered (Baars 2013).

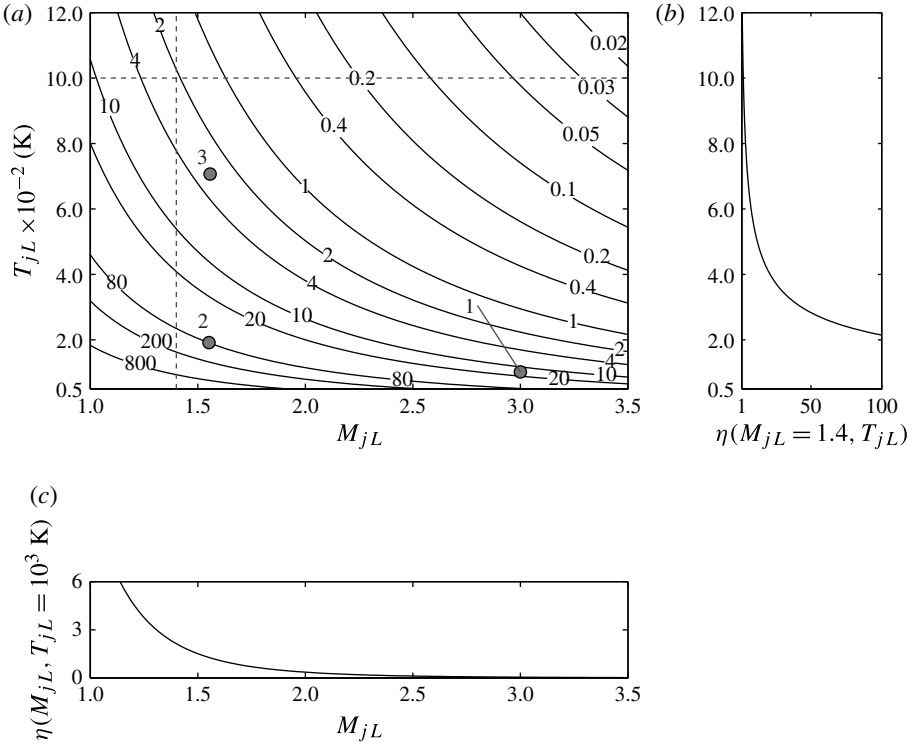

FIGURE 15. (*a*) Parameter η for the scaling of the spherical shock formation distance for supersonic jets relative to a full-scale reference case ($M_{jF} = 1.4$, $T_{jF} = 10^3$ K). Conditions of the current study (point 1) along with the unheated (point 2) and heated (point 3) jet conditions from Baars *et al.* (2011) are indicated by the solid circles. (*b*) η for fixed $M_{jL} = 1.4$, (*c*) η for fixed $T_{jL} = 10^3$ K, identified by dashed lines in (*a*).

In figure 15, the parameter η resides within roughly two orders of magnitude for a wide range of laboratory operating conditions. Furthermore, when the laboratory experiment encompasses an unheated and low-Mach-number jet, η becomes significantly large. This is the first indicator that studying cumulative nonlinearities in range-restricted environments is not necessarily feasible when the jet is operated under these conditions. Namely, if η becomes large, $\bar{r}_L/D_{jL}$ becomes extensively large (although the source size factor becomes much smaller than one). Shock formation (in an ideal lossless world) is thus expected to occur far outside any practical laboratory-scale anechoic environment. As a final indication of the usefulness of these scaling laws, it can be shown that when $\eta = 1$, it follows from (4.16) that the shock formation distance scales geometrically:

$$\frac{\bar{r}_L}{D_{jL}} = \frac{\bar{r}_F}{D_{jF}}. \tag{4.17}$$

4.4. *Scaling the effective Gol'dberg number for spherical waves*

Upon learning the effect of jet exit conditions on shock formation distance, it is natural for one to inquire about how these conditions can impact on the effective Gol'dberg number Λ. This ultimately determines to what extent, and in what

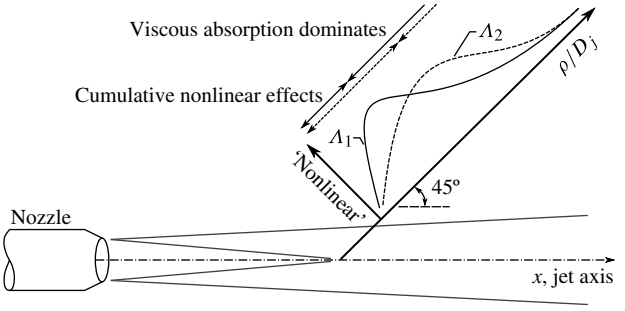

FIGURE 16. Illustration of the qualitative picture of nonlinearities along a ray for two different effective Gol'dberg numbers: $\Lambda_1 > \Lambda_2$ (not to scale).

range, cumulative nonlinear waveform distortions become pronounced. A simplified illustration of the effect of Gol'dberg number on the degree of cumulative nonlinear distortion to the waveform emanating from the point of maximum OASPL is illustrated in figure 16. One may choose to consider these two trends representative as of the amplitude of the second (or higher-order) harmonics in the case of a mono-frequency source. Or, with the current study in mind, figure 16 would illustrate increases in energy in the high-frequency bands of the SPL (relative to a base case) since steepened signals encompass more high-frequency energy. Nevertheless, an initial rise in the waveform distortion due to cumulative nonlinear effects (waveform becomes more nonlinear) eventually plateaus and reaches its maximum value when viscous absorption becomes dominant. Viscous absorption continues to relax any further distortions and so the degree of nonlinearity eventually decreases asymptotically with propagation distance. When the effective Gol'dberg number is smaller (dashed curve relative to solid curve), wave steepening develops less rapidly.

Ideally, one would prefer to match laboratory- and full-scale scenarios where the relationship between the degree of cumulative nonlinearity and ρ/D_j is concerned. This would ensure that the wave steepening process (and possible shock formation and coalescence) occurs at similar positions along the propagation path. Only then will an interpretation of sub-scale results be valid for the corresponding full-scale conditions. And so, it is in one's interest to hold ΛD_j constant, or at least within the same order of magnitude (given the assumptions in this model discussed earlier).

Here we now explore whether cumulative nonlinear distortions to the acoustic waveform produced in the current laboratory-scale environment can be used to predict the same type of distorted waveform observed in full-scale tests, or under what conditions might one be able to replicate the full-scale distorted waveform in a range-restricted environment. The mathematical expressions for this are relatively straightforward. From (4.9) and (4.16), it can be shown that

$$\frac{\Lambda_F}{\Lambda_L} = \frac{\alpha_L}{\alpha_F}\frac{\bar{x}_L}{\bar{x}_F}\exp\left((\bar{x}_L/r_{0L}) - (\bar{x}_F/r_{0F})\right) \tag{4.18}$$

which can be rewritten as

$$(\Lambda_F D_{jF}) = (\Lambda_L D_{jL})\eta\frac{\alpha_L}{\alpha_F}\exp\left((\bar{x}_L/r_{0L}) - (\bar{x}_F/r_{0L})\right). \tag{4.19}$$

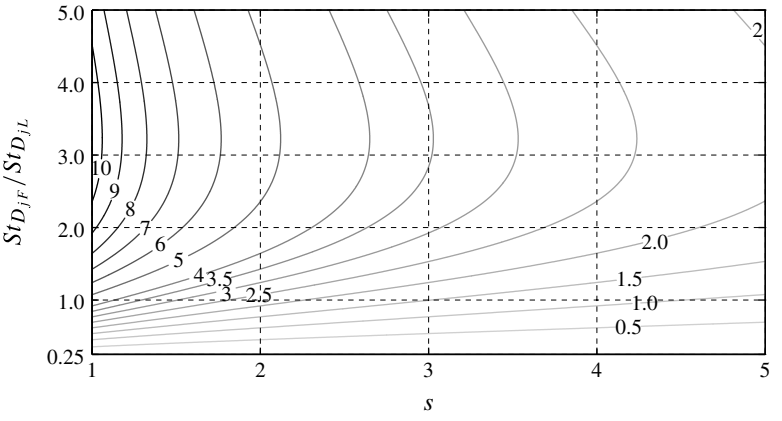

FIGURE 17. Effective Gol'dberg number for the full-scale case as predicted by the model: $\Lambda_{Fm}(s, St_{D_{jF}}/St_{D_{jL}})$ (multiply contour values by 10^3).

It is preferred to express the ratio α_L/α_F in terms of jet parameters, which could be achieved by using an absorption coefficient comprising only thermoviscous effects; see (4.2). However, since vibrational states of the molecules form unique asymptotes that differ between laboratory- and full-scale scenarios (differences in peak Strouhal numbers may be large; see figure 12*b*), classical absorption alone is incapable of furnishing an accurate comparison between the two scenarios. Thus, in order to compute parameter group (ΛD_j) for the full-scale case based on known laboratory-scale values (or vice versa), (4.19) is used directly.

With this approach in mind, an attempt is made to predict the effective Gol'dberg number of the full-scale conditions, based on the model and the current laboratory-scale conditions (denoted by the subscript 'Fm', see the schematic in figure 13), and is shown in figure 17. The model prediction (Λ_{Fm}) is dependent on the emission-point location and full-scale Strouhal number corresponding to the peak frequency in the direction of maximum OASPL. Once again, since the effect of Mach number and temperature ratio on the peak Strouhal number is unknown at this time, a range of possible solutions based on $St_{D_{jF}}/St_{D_{jL}}$ should be considered.

Choosing now to isolate a peak Strouhal number for the full-scale condition (based on the measurements of Gee *et al.* 2012), the effect of source size on Λ_{Fr} can be determined, as is shown in figure 18(*a*) for the appropriate choice of $St_{D_{jF}}/St_{D_{jL}}$. Here, the Gol'dberg number for the full-scale condition, predicted by the model and based on laboratory-scale conditions, is approximately 1260 times higher than the laboratory value. On the contrary, if we choose to fix the emission-point scale ($s = 2.5$), the effect of Strouhal number on the Gol'dberg ratio can be determined, as is shown in figure 18(*b*). The decay in Gol'dberg number above $St_{D_{jF}}/St_{D_{jL}} = 2.5$ is a consequence of increased absorption at higher frequencies.

In an effort to determine the validity of this model approach, the effective Gol'dberg number is computed for the full-scale study of Gee *et al.* (2012), and compared to the prediction based on laboratory-scale conditions. The same approach for estimating nonlinear characteristic parameters is applied to the full-scale conditions whereby the OASPL at the emission point is obtained by extrapolating near-field observer levels to an imaginary point at r_0 with corrections for atmospheric absorption. The resultant full-scale effective Gol'dberg number is shown in figure 18(*a*) and is approximately

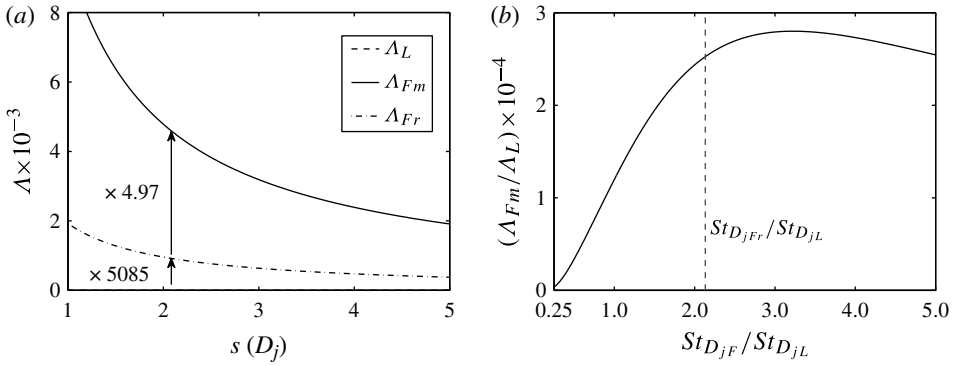

FIGURE 18. (*a*) Effective Gol'dberg number for the laboratory case (Λ_L), the full-scale model prediction (Λ_{Fm}) and the full-scale measurement (Λ_{Fr}), note that the dashed line (indicating Γ_L) is not visible due to its low amplitude. (*b*) Ratio of the predicted full-scale and laboratory Gol'dberg number as function of Strouhal number ratio.

Case		l_a (m)	$\bar{x}$ (m)	$\bar{r}$ (m)	$\bar{r}/D_j$	Λ	ΛD_j (m)
(*a*)	Lab. (current data)	385	0.36	18.0	708	0.150	0.004
(*b*)	Full (Gee *et al.* 2012)	6738	2.13	5.83	6.13	764.1	725.8
(*c*)	Full (model, $I \propto U_j^8$)	6738	0.95	3.72	3.92	3821	3630
(*d*)	Full (model, $I \propto U_j^3$)	6738	2.44	6.98	7.35	550.9	523.4

TABLE 4. Nonlinear characteristic parameters for the: (*a*) laboratory-scale case computed from current measurements, (*b*) full-scale computed directly from measurements of Gee *et al.* (2012), (*c*) full-scale predicted from laboratory-scale conditions using the presented model, and (*d*) similar to case (*c*), but assuming $I \propto U_j^3$. The emission-point scale is $s = 2.5$.

five times lower than the model prediction. A summary of the nonlinear parameters is provided in table 4 based on a typical emission-point scale of $s = 2.5$. Additionally, the model predictions were recalculated assuming $I \propto U_j^3$, following the work presented by Ffowcs Williams (1963). The results of this are presented in case (*d*) of table 4. When comparing the values to cases (*b*) and (*c*), it can be concluded that nonlinear parameters are of the same order of magnitude.

This model is scrutinized further by considering the laboratory-scale study of Baars *et al.* (2011) comprising a heated ($T_0 = 1020.6$ K and $T_j = 706.6$ K) fully expanded Mach 1.553 jet, with an exit diameter of $D_j = 50$ mm. The measurement along the peak noise direction (also at around 45°) is located at $\rho/D_j = 58.5$. The OASPL was measured to be 138.20 dB with a centre frequency of 3 kHz. The full-scale parameters predicted by these new laboratory-scale conditions are summarized in table 5. Like table 4, the results of table 5 appear to be within an acceptable range (i.e. same order of magnitude) where a prediction of the shock formation distance and effective Gol'dberg number are concerned. The same exercise was repeated with a different full-scale reference study and resulted in predicted values of similar accuracy; this is summarized by Baars (2013).

While we consider these results to be good, we prefer to offer a number of plausible reasons for the discrepancies in case one might wish to improve on this first principles approach. Foremost, the dependence of the emission-point scale s

Case		l_a (m)	$\overline{x}$ (m)	$\overline{r}$ (m)	$\overline{r}/D_j$	Λ	ΛD_j (m)
(*a*)	Lab. (Baars *et al.* 2011)	582	0.54	9.72	195	1.146	0.057
(*b*)	Full (Gee *et al.* 2012)	6738	2.13	5.83	6.13	764.1	725.8
(*c*)	Full (model, $I \propto U_j^8$)	6738	4.16	14.4	15.1	103.7	98.55
(*d*)	Full (model, $I \propto U_j^3$)	6738	4.92	19.8	20.9	52.95	50.30

TABLE 5. Similar to table 4, but for the laboratory measurements of the heated jet presented by Baars *et al.* (2011).

on exit Mach number and exit temperature ratio is unknown and may result in large differences between laboratory-scale and full-scale conditions. Furthermore, the source intensity relationship for high-Mach-number and high-temperature-ratio nozzles (rockets) is not clearly known and may resemble more the trends presented by Ffowcs Williams (1963). Likewise, the decay in sound intensity near the source obeys cylindrical spreading ($p \propto 1/\sqrt{\rho}$). This has an added effect of reducing the intensity at the emission point ($s = 2.5$), and further extending the shock formation distance. Nevertheless, insightful conclusions can be drawn here. Foremost, the parameter group (ΛD_j) being more than three orders of magnitude lower in the laboratory-scale case suggests that cumulative nonlinear distortions in the acoustic waveform will be more distinct under full-scale conditions, as opposed to measurements performed in a range-restricted environment. For instance, the increased peak frequency has a profound influence on the Gol'dberg number due to increased absorption. This further delays the shock formation which makes it more difficult to capture and study cumulative nonlinear distortions in a range-restricted environment. Finally, cumulative nonlinear effects are expected to form in the waveforms emitted by this unheated Mach 3 jet flow. However these distortions are not expected to appear significant in the region where our measurements are being conducted, given the spatial confines of our anechoic chamber. Thus, no major wave steepening and coalescence are expected to be observed, as will be shown in the next section.

5. A statistical description of the acoustic field

We begin with a correlation study along our line-array in § 5.1 to verify the propagation path of noise produced by this jet flow. Various statistical metrics are then used in § 5.2 to quantify the degree of both local and cumulative nonlinear distortion, which includes a waveform propagation study using the generalized Burgers equation.

5.1. *Spectral statistics along the propagation path*

If the propagation path is unknown, one may inadvertently link differences between the measured and linearly projected far-field spectra to cumulative nonlinear effects; this problem has been addressed only recently (Kuo *et al.* 2012; Baars 2013; Baars & Tinney 2014). As an illustration, spectra along lines C and H (see figure 5) are presented in figure 19(*a*) (all scaled to $\rho/D_j = 100$ using linear spreading). While the spectra along line C collapse, it is clear that they do not along line H. This is simply because the noise does not propagate along line H, and so different features of the far-field pressure waveform from various angles are observed instead of just one propagation angle. This example shows the importance of having sufficient knowledge about the spatial dependence of the sound field, as opposed to single point measurements far from the jet. From the spectra along the line-array (figure 10*a*) it

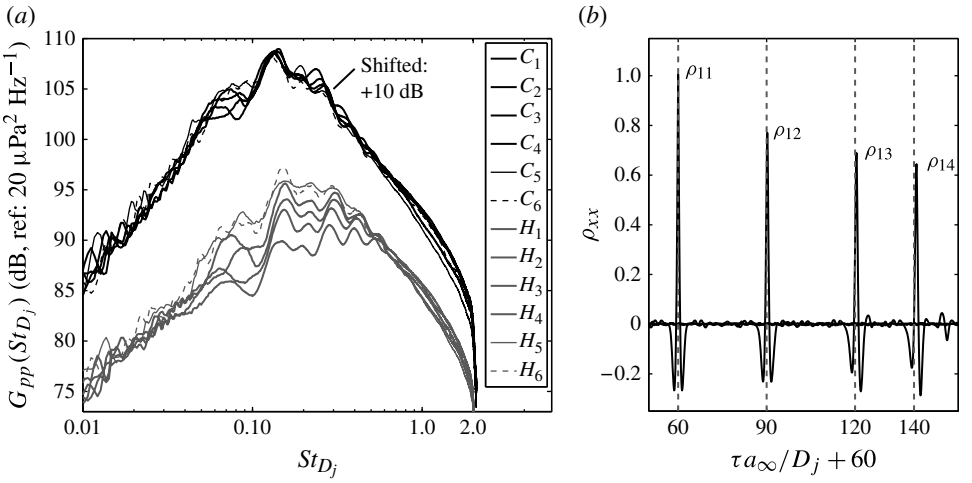

FIGURE 19. (*a*) PSDs along lines C (black lines) and H (grey lines) after being linearly scaled to $\rho/D_j = 100$ (centred on $x = 0$ for line H and $x/D_j = 20$ for line C) (5 % bandwidth moving filter). (*b*) The temporal cross-correlation coefficient between the first and subsequent microphones on the line-array.

is clear that there is no significant increase in the high frequencies and so it is assumed that cumulative nonlinear distortion is too weak or non-existent in this region. Cross-correlations between the first ($60D_j$) and three subsequent microphones are presented in figure 19(*b*) to show the arrival times of the acoustic disturbances along the line-array. The high correlation coefficients ($0.64 < \rho_{xx} < 0.77$), suggest that distortions are weak along this path, since they would have been expected to cause a more significant loss of linear coherence (Ffowcs Williams *et al.* 1975).

5.2. *Metrics for quantifying nonlinearities*

Various statistical metrics have been used in the past to locally characterize the degree of nonlinearity in a waveform (Gallagher & McLaughlin 1981). The spatial topography of these localized nonlinear indicators can be used to infer information about cumulative distortions in that region, as is done here. We begin with the third and fourth central moments of the pressure waveform $p(t)$, and its derivative $\dot{p}(t)$, which are used to characterize deviations from a Gaussian process and are presented in non-dimensional form as skewness (S) and kurtosis (K). For the pressure waveform, these are defined as $S(p) = \overline{p^3}/\sigma^3$ and $K(p) = \overline{p^4}/\sigma^4$, where σ is the variance of $p(t)$, $\overline{p^3}$ and $\overline{p^4}$ are the third and fourth central moment of the p.d.f. respectively (Tennekes & Lumley 1972). Additional indicators include the wave steepening factor (WSF) and the Morfey–Howell indicator. The first of these is defined as the modulus of the average negative slope divided by the average positive slope in the waveform (Gallagher & McLaughlin 1981). The range of WSF is thus [0, 1], where 1 corresponds to a pure harmonic wave and zero to a perfect N wave. The Morfey–Howell indicator has become an increasingly popular approach in the jet noise community for those interested in studying cumulative nonlinear acoustic waveform distortions. Applications can be found in the literature (McInerny & Ölçmen 2005; Petitjean *et al.* 2006; Kuo *et al.* 2010). Originally derived by Morfey & Howell

(1981), this indicator starts with a statistical from of the Burgers equation

$$\frac{\partial}{\partial r}\left[r^2 \mathrm{e}^{2\alpha r} S_{pp}(r,f)\right] = -2\pi f \frac{\beta}{\rho_\infty c_\infty^3} \mathrm{e}^{2\alpha r} Q_{p^2p}(r,f), \tag{5.1}$$

where r is the coordinate along the propagation path, S_{pp} is the double-sided PSD of the pressure, and Q_{p^2p} is the quadrature spectral density, which is the imaginary part of the conjugated single-sided cross-spectral density between the pressure squared and the pressure (Bendat & Piersol 1980):

$$Q_{p^2p}(f) = -\mathrm{Im}\left[2P_2(f)P^*(f)\right]. \tag{5.2}$$

Here, $P(f)$ and $P_2(f)$ are the Fourier transforms of the signals $p(t)$ and $p^2(t)$ respectively. The factor two accounts for the single-sided version of the PSD. The spatial rate of change of the PSD, involving linear spreading and atmospheric absorption, appears on the left-hand side of (5.1) and would be zero in the case of linear spreading. A logical step forward is to argue that the right-hand side accounts for nonlinear distortion of the spectrum (Morfey & Howell 1981). Thus, any nonlinear distortion must be the consequence of a non-zero value of the quadrature spectral density. In the case of a positive right-hand side (for certain frequencies), the PSD on the left-hand side gains energy in that frequency band due to nonlinear distortion, and vice versa for a negative right-hand side. Equation (5.1) can be thought of as being analysed between two points (Δr apart from each other) on a propagation path. In practice, the right-hand side is computed at a single point and so the left-hand side is the derivative at that point in the limit of small Δr. Here we choose to consider the normalized form of the quadrature spectral density,

$$Q(f) = \frac{Q_{p^2p}(f)}{p_{rms}^3}, \tag{5.3}$$

which has dimensions of Hz^{-1}. One of the most used forms of the indicator has been introduced as Q/S and uses the PSD to obtain a dimensionless quantity:

$$\frac{Q}{S}(f) = \frac{Q_{p^2p}(f)/p_{rms}^3}{S_{pp}(f)/p_{rms}^2}. \tag{5.4}$$

Once again, the indicator can only measure how the energy in the PSD is redistributed due to cumulative nonlinear distortion effects when multiple points on a spreading ray are analysed. As an example, Q and Q/S are shown in figure 20 for arc-array microphone 5. The trends are relatively similar, as is expected given that S is positive-definite. However, Q/S increases quite significantly at higher frequencies due to the roll-off of the PSD. Overall, both Q and Q/S exhibit the same features that are required of this study. However, an exact interpretation of the amplitude of the indicator, as well as its physical meaning, is problematic for those working with this technique.

Before proceeding further, it is important to emphasize the nonlinear detection characteristics of this single-point indicator. Foremost, the quadrature spectral density Q_{p^2p} is zero for a truly Gaussian signal. This is assumed to be the case for the noise source in the above discussion. Therefore, when a Gaussian acoustic waveform propagates away from its source, it may distort and become non-Gaussian due

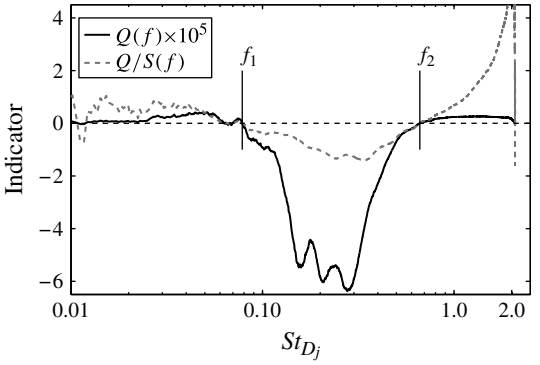

FIGURE 20. The normalized quadrature spectral density Q (in Hz^{-1}), and the Q/S Morfey–Howell indicator for arc-array microphone 5.

to nonlinearities. The single-point Morfey–Howell indicator detects this as being non-zero and so one concludes that the waveform has undergone cumulative nonlinear distortion between the source region and observer location. However, no distinction can be made between local effects, cumulative effects, or a combination of the two based on a single-point measurement alone (Howell & Morfey 1987). It is further pointed out that the quadrature spectral density is highly sensitive to deviations from a Gaussian, which may be an unavoidable consequence of instrument errors or the averaging process.

To demonstrate this, an arbitrarily chosen, and experimentally acquired, waveform is selected from a jet noise data set to form the basis for the simulated data. Since it is preferred to start with a characteristic jet noise signal that was subject to minimal wave steepening, a pressure waveform is extracted from the unheated jet study presented by Baars *et al.* (2011). The far-field pressure waveform at $\rho/D_j = 58.5$ and $\theta = 20°$ is considered; its time series was sampled at 200 kHz and includes a total of 2^{21} samples. The spectrum peaks at a centre frequency of $f_0 = 1.2$ kHz. The signal is projected to several observer positions using the numerical algorithm presented by Gee (2005). The algorithm is an extended version of the seminal work presented by Pestorius & Blackstock (1974). The simulation is performed with typical atmospheric conditions ($T_\infty = 288.0$ K, $p_\infty = 1$ atm, RH = 40 %, $\rho_\infty = 1.226$ kg m^{-3}, $a_\infty = 340.2$ m s^{-1}, $\beta = 1.201$) and with a large source amplitude at $r = 3$ m ($p_{rms} = 582.4$ Pa, or 149.3 dB, $p_{ref} = 20 \times 10^{-6}$ Pa) to ensure sufficient waveform steepening. The algorithm assumes that the fluid is lossless (no viscous absorption) and plane wave propagation is used for practical purposes so that the resultant shock formation distance is estimated from (4.3) to be $\bar{x} = 9.2$ m.

Four of the projected waveforms $p(t)$ at $r = [4, 6, 8, 10]$ m are shown in figure 21 along with the original input waveform ($r = 3$ m) and the corresponding time derivatives $\dot{p}(t)$; derivatives are computed using a first-order forward difference routine. PSDs, quadrature spectral densities and the Morfey–Howell indicator of these projected waveforms are shown in figure 22 alongside the quantity associated with the input waveform at $r = 3$ m (dashed line). Statistical attributes of the evolving waveform and its temporal derivative, are inspected by way of its p.d.f., skewness and kurtosis, and are listed in table 6.

In figure 21(*a*,*b*) the waveform is shown, as expected, to undergo wave steepening, shock formation and eventual coalescence with increasing distance from the source.

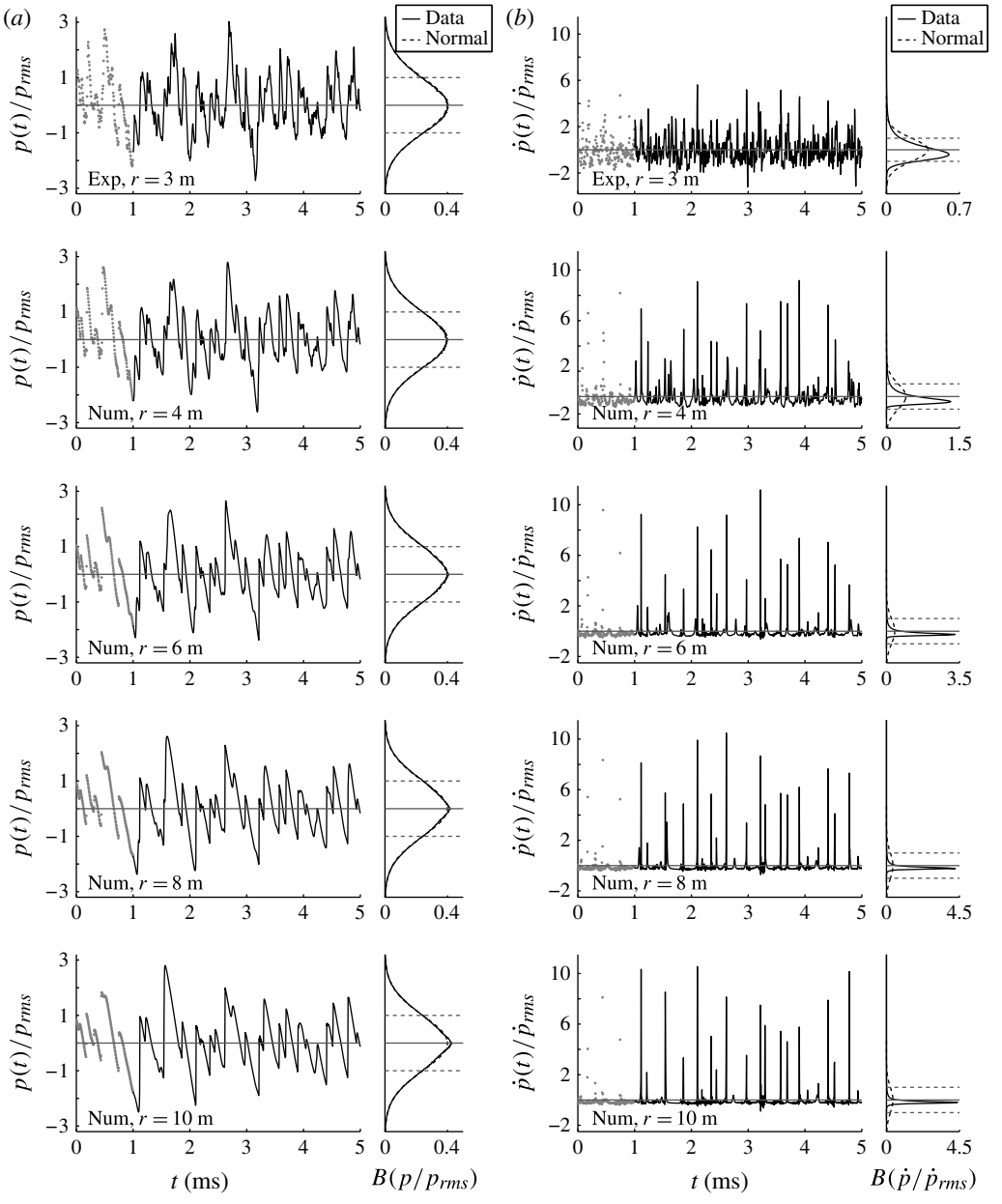

FIGURE 21. Waveform projections using the generalized Burgers equation, at various radial distances as indicated. (*a*) The raw waveform and (*b*) its temporal derivative.

The p.d.f. of $p(t)$, indicated by the symbol B, shows negligible deviations from a Gaussian whereas $\dot{p}(t)$ manifests deviations which increase significantly with increasing distance. For the spectral behaviour of the waveform in figure 22(*a*), shifts in energy from mid to high frequencies are observed and crossover frequencies increase with incremental distances from the source. This upward shift in energy is a well-known consequence of waveform steepening. Likewise, $Q(f)$ and $Q/S(f)$ for the input waveform are non-zero in figure 22(*b*,*c*), thus demonstrating the acute

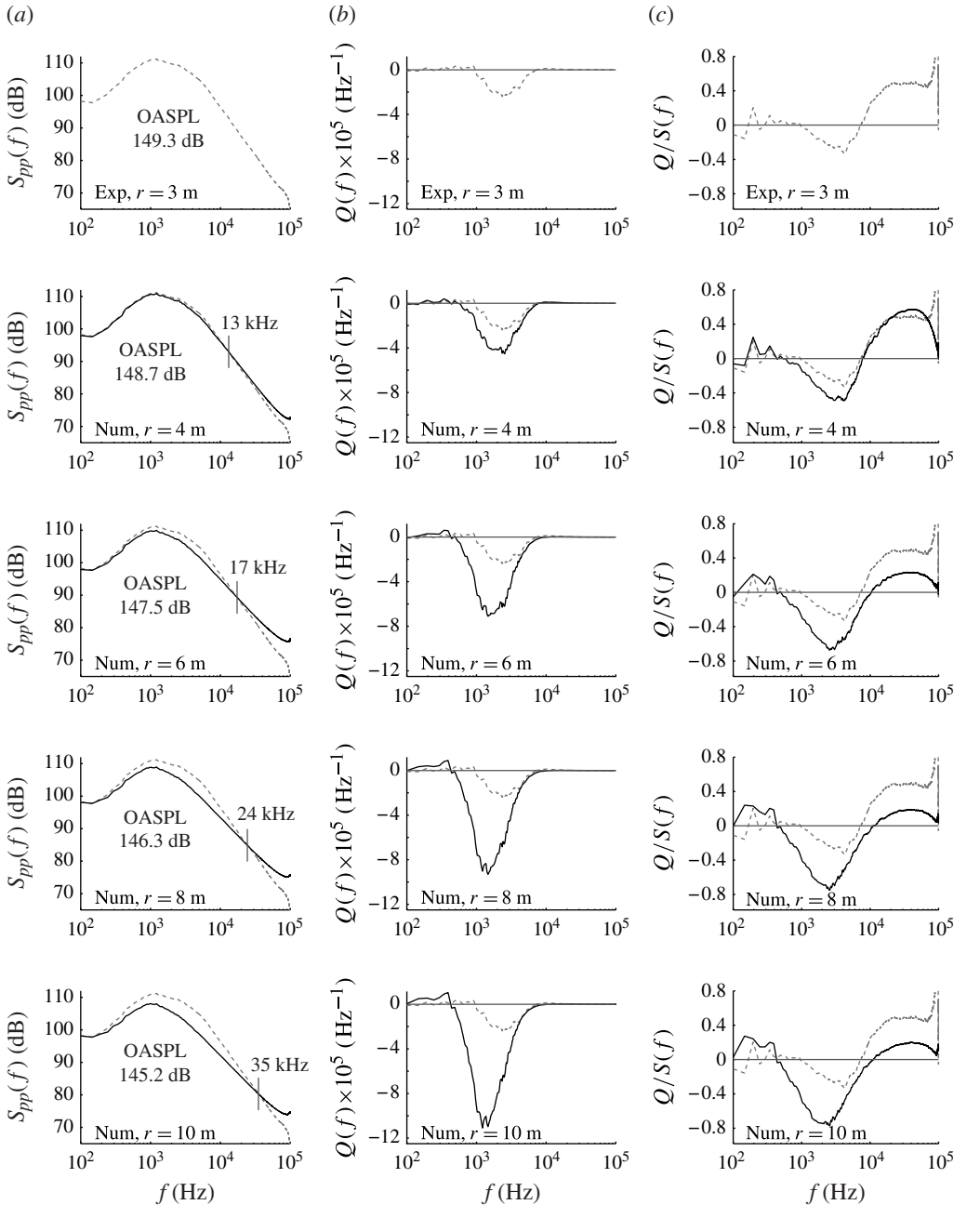

FIGURE 22. (*a*) PSDs, (*b*) normalized quadrature spectral density Q and (*c*) the Q/S Morfey–Howell indicator applied to the waveform data in figure 21.

sensitivity of these parameters to the p.d.f. of the signal. This non-zero quadrature spectral density and Morfey–Howell indicator at the $r = 3$ m observer position is a testament to the necessity of measuring these properties at several positions along the propagation path (as opposed to just one) if one is to accurately characterize the degree of cumulative nonlinear distortion to the far-field acoustics from jet flows,

r (m)	OASPL (dB)	$S(p)$	$S(\dot{p})$	$K(p)$	$K(\dot{p})$	WSF
3	149.3	0.095	2.529	3.062	19.25	0.669
4	148.7	0.037	7.438	2.930	92.50	0.433
6	147.5	−0.004	8.648	2.864	96.59	0.252
8	146.3	−0.010	8.790	2.895	97.03	0.201
10	145.2	−0.006	9.047	2.948	102.68	0.182

TABLE 6. Statistical properties of the raw and projected waveforms displayed in figure 21(a).

since the statistical nature of the source is most often unknown. Thus, a non-zero quadrature spectral density observed from a single-point measurement alone may inadvertently compel one to believe that a cumulative nonlinear distortion process is perceived.

Morfey & Howell (1981) have suggested that for aircraft noise prediction studies, it is preferable to integrate Q/S along the propagation path in order to characterize the net flux of energy transfer. Here we have chosen to confine the limits of integration to the negative part of the quadrature spectral density, i.e.

$$Q_{neg} = \int_{f_{neg}} Q(f)\mathrm{d}f, \tag{5.5}$$

which, in practice, involves integrating from f_1 to f_2 in figure 20. Table 7 displays the results of applying (5.5) to the sample waveforms. As expected, a clear change in the net flux is manifested, which is due to the cumulative nonlinear waveform distortion.

5.2.1. *Application to the far-field of the Mach* 3 jet

Having reviewed how the quadrature spectral density and other statistical metrics are affected by cumulative nonlinear waveform distortions, the next step is to apply the same analysis methods to the current data set of our Mach 3 jet flow. It is important to note that the pressure time series of the current study were high-pass filtered at 400 Hz to ensure that slow drifts in the microphone signal and equipment were not saturating any result of the skewness and any other statistical metric. Figure 23 depicts estimates of Q and Q/S from the microphone signals along spreading lines A to G as they emanate from the post-potential-core regions of the flow. It is clear that each spreading line exhibits a unique trend for both Q and Q/S and that their amplitudes are greatest at shallower angles. This implies that nonlinearities in the pressure signals are strongest within the Mach cone. Further, for a given spreading line, the trends collapse quite well, which suggests that the propagation path has been correctly identified; had line H been chosen from figure 5, false conclusions would be formed regarding the presence of cumulative nonlinearities. Contours of Q_{neg} from the Mach 3 jet data are also shown in figure 24(*a*); note that contours of $(Q/S)_{neg}$ result in a similar topography. The angle at which the maximum negative values occur is slightly steeper than the estimated Mach wave radiation angle, but continues along a path emanating from the post-potential-core regions of the flow.

From figures 23(*a*,*b*) and 24(*a*), a number of important conclusions can be made about the use of the Morfey–Howell indicator for characterizing either local or cumulative nonlinear distortions in the waveform. Negligible changes are observed in Q and Q/S over the propagation paths emanating from the post-potential-source

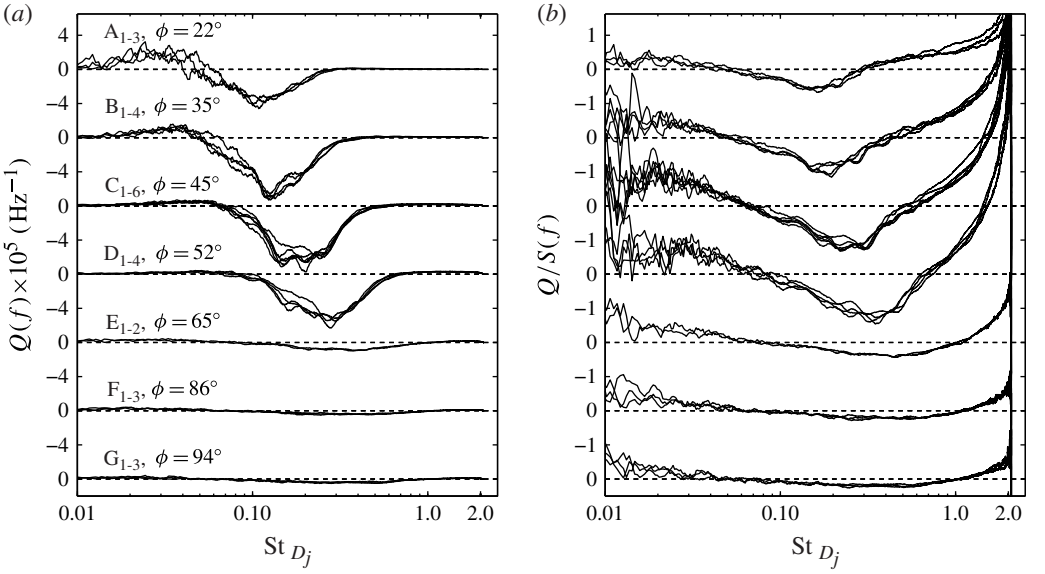

FIGURE 23. (*a*) The quadrature spectral density, and (*b*) the normalized quadrature spectral density along the spreading lines A–G (5 % bandwidth moving filter).

r (m)	$-Q_{neg}$	$-(Q/S)_{neg} \times 10^{-3}$ (Hz)
3	0.072	1.156
4	0.139	2.196
6	0.196	3.204
8	0.220	3.440
10	0.235	3.426

TABLE 7. Metrics corresponding to the spectra of the raw and projected waveforms displayed in figure 22(*b*,*c*).

region which suggests that if the waveform is undergoing cumulative distortions, the process is very slow to form in this region and that the shock formation distance is much further out than our farthest measurement. This provides evidence that earlier estimates for the shock formation distance are indeed correct; our model estimates $\bar{r}_L = 18.0$ m and $\Lambda_L = 0.15$ for $s = 2.5D_j$. While our measurements extend to $140D_j$ from the source, they are still confined by the restrictions of the chamber walls which only extend to about 3.5 m; this is approximately 20 % of the estimated shock formation distance. Figure 23(*a*,*b*) is the first real demonstration that little to no measurable cumulative nonlinear distortions are present in this region of the far-field even though single-point Q and Q/S indicators are non-zero.

Contours of WSF, skewness of the pressure time series and skewness of the pressure time derivative are shown in figure 24(*b–d*), respectively. The contour levels have been normalized as described in the captions, so that their ranges fall between 0 and 10. Illustrating them in this way means that a higher number indicates more nonlinearities in the waveform, or shock-type structures in the waveform. The topography of these metrics indicates how waveforms are most steepened along the

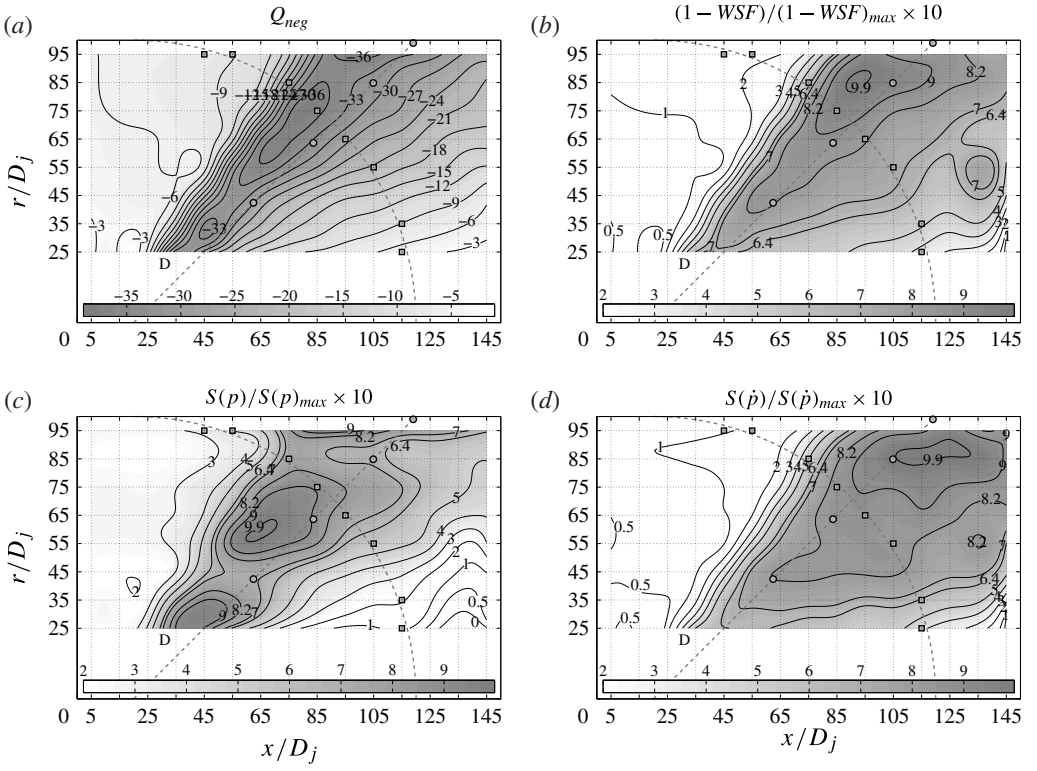

FIGURE 24. Contours of (*a*) Q_{neg}, (*b*) WSF, where $(1-\mathrm{WSF})_{max}=0.36$ at $(x,\,r)/D_j=(95,\,85)$, (*c*) pressure skewness, where $S(p)_{max}=0.47$ at $(x,\,r)/D_j=(65,\,55)$ (contours of $S(p)=0.3$: contour line 6.4, and $S(p)=0.4$: contour line 8.2 is indicated as well), and (*d*) skewness of the pressure derivative, where $S(\dot{p})_{max}=1.96$ at $(x,\,r)/D_j=(115,\,85)$. Subfigures (*b*), (*c*) and (*d*) are taken from Baars & Tinney (2014).

Mach wave radiation angle with lines closely aligned with the direction of highest sound intensity. A steep inclination is observed for all criteria which resembles the trend observed for the OASPL (figure 6). Although the trends are globally similar for all criteria, there are subtle differences in the location of the peak values. The physical relevance of the node at $(x,\,r)/D_j=(135,\,55)$ is questionable given the proximity of the wind tunnel collector to this measurement location. And so, aside from the lack of significant waveform steepening, shock coalescence also appears to be absent in our measurement region. A summary of these nonlinear indicators along the arc-array is listed in table 8 for reference. This clearly indicates that the skewness of the pressure derivative is more sensitive to these nonlinear, shock-type waveform structures, as was demonstrated by McInerny (1996).

6. Summary and conclusions

The acoustic field of an unheated and perfectly expanded Mach 3 jet flow was examined to understand the degree of local and cumulative nonlinear waveform distortion of sound produced by high-speed jets. The source mechanisms of interest are those produced by the formation of Mach waves which propagate significantly from regions that are known to be confined to boundaries defined by the potential core and supersonic core lengths.

Mic. no.	OASPL (dB)	$S(p)$	$S(\dot{p})$	WSF	$-Q_{neg}$
1	129.5	0.047	0.828	0.867	0.047
2	130.9	0.069	1.234	0.812	0.089
3	133.8	0.281	1.657	0.736	0.206
4	135.5	0.371	1.720	0.697	0.280
5	135.4	0.435	1.673	0.657	0.368
6	131.6	0.371	0.973	0.778	0.261
7	125.5	0.177	0.231	0.941	0.089
8	124.7	0.144	0.177	0.956	0.073

TABLE 8. Metrics corresponding to the microphones on the artificial arc-array.

A model for predicting the formation of cumulative nonlinear distortions to acoustic waveforms produced by jets has been proposed, and comprises a reformulation of expressions for shock formation distance and an effective Gol'dberg number in terms of jet parameters of practical interest. This includes typical effects imposed by jet Mach number, temperature ratio, and Strouhal number of the peak frequency being along the peak noise emission path. Laboratory-scale measurements of the Mach 3 jet are used in conjunction with full-scale tests documented in the literature to justify the findings of this model. Two different scaling scenarios are then presented for the practising scientist to choose from. The first of these allows shock formation distance to be preserved between laboratory and full-scale conditions based on a geometric scaling of the shock formation distance using nozzle diameter. The second scenario allows one to preserve the wave steepening process between laboratory and full-scale conditions based on a match of the effective Gol'dberg number.

There are, of course, several opportunities for improving upon this model by developing a more thorough assessment of how jet exit conditions affect scaling parameters. Where Strouhal number is concerned, it is still unclear how the peak frequency along the dominant sound propagation path depends on jet exit conditions such as temperature ratio or Mach number. It is also assumed here that the location from where the waveform is emitted scales with nozzle diameter only. This assumption disregards the dependence of the emission-point location size on Mach number, Reynolds number, temperature ratio, or even the operating state of the nozzle (overexpanded or underexpanded). For overexpanded and underexpanded jets, broadband shock noise is saturated by turbulent mixing noise along shallow angles to the jet axis (within the Mach cone of the jet) so measurable distortions of the acoustic waveform are still anticipated for supersonic jets operating under off-design conditions so long as the effective Gol'dberg number is shown to be sufficiently large. Deficiencies in our understanding of these dependences would be alleviated by accurate parameterization of the effects of Strouhal number and source size on Mach number, temperature ratio and Reynolds number. Finally, and most importantly, it is unclear what effect a pre-steepened acoustic waveform has on shock formation distance. Waveform steepening occurs when the wave amplitude is large enough to overcome viscous absorption. This requires a large source intensity and, hence, a high Mach number at the exit. This suggests that cumulative nonlinear acoustic distortions are unlikely to occur under subsonic jet exit conditions. However, viscous absorption is considerably weaker at low frequencies, and so it is still plausible for a geometrically large subsonic flow to produce acoustic waves capable of undergoing cumulative nonlinear distortions. Nevertheless, Mach waves that develop in supersonic

jets produce pre-steepened waveforms and thereby accelerate the wave steepening process and shorten the shock formation distance. A documented execution of the generalized Burgers equation using pre-steepened waveforms could provide useful answers to this last concern.

Temporal waveforms from the Mach 3 jet study are then examined using various statistical metrics including skewness, kurtosis, WSF and the Morfey–Howell nonlinearity indicator. For the Morfey–Howell indicator, it is demonstrated that the spatial evolution of this metric, along a path resembling a $p \propto 1/r$ decay law, should only be considered, due to the problematic interpretation of its amplitude as well as the highly directive nature of the sound field produced by jets; similar concerns have been reported only recently by others (Kuo *et al.* 2012; Baars 2013). This is especially important for problems in jet noise where the statistical nature of the source term is unknown.

Acknowledgements

The authors gratefully acknowledge support from the Air Force Office of Scientific Research under grant number FA9550-11-1-0203, Dr John Schmisseur, program manager, and the Office of Naval Research, ONR award number N00014-11-1-0752, Dr Joseph Doychak and Dr Brenda Henderson, program managers. We would also like to give special thanks to Brian W. Donald, Lauren J. Cooper and Alexis Avram for their assistance during the experiments, and to Bernie J. Jansen and Dr Nathan E. Murray for providing the Mach 3 nozzle contour. The ideas developed here are a culmination of discussions that have transpired over several years between the authors and Dr David T. Blackstock, Dr Philip J. Morris and Dr Dennis K. McLaughlin.

REFERENCES

BAARS, W. J. 2013 Acoustics from high-speed jets with crackle. PhD thesis, The University of Texas at Austin, Austin, TX.

BAARS, W. J. & TINNEY, C. E. 2013 Transient wall pressures in an overexpanded and large area ratio nozzle. *Exp. Fluids* **54** (2), 1–17.

BAARS, W. J. & TINNEY, C. E. 2014 Shock-structures in the acoustic field of a Mach 3 jet with crackle. *J. Sound Vib.* **333** (12), 2539–2553.

BAARS, W. J., TINNEY, C. E., MURRAY, N. E., JANSEN, B. J. & PANICKAR, P. 2011 The effect of heat on turbulent mixing noise in supersonic jets. *AIAA Paper* 2011-1029.

BENDAT, J. S. & PIERSOL, A. G. 1980 *Engineering Applications of Correlation and Spectral Analysis*. Wiley.

BLACKSTOCK, D. T. 2000 *Fundamentals of Physical Acoustics*. John Wiley & Sons.

CRIGHTON, D. G. 1986 *Nonlinear Acoustic Propagation of Broadband Noise* (ed. A. Krothapalli & C. A. Smith), pp. 411–454. Springer.

CRIGHTON, D. G. & BASHFORTH, S. 1980 Nonlinear propagation of broadband jet noise. *AIAA Paper 1980-1039*.

FFOWCS WILLIAMS, J. E. 1963 The noise from turbulence convected at high speed. *Phil. Trans. R. Soc. Lond.* A **255**, 469–503.

FFOWCS WILLIAMS, J. E. & MAIDANIK, G. 1965 The Mach wave field radiated by supersonic turbulent shear flows. *J. Fluid Mech.* **21**, 641–657.

FFOWCS WILLIAMS, J. E., SIMSON, J. & VIRCHIS, V. J. 1975 'Crackle': an annoying component of jet noise. *J. Fluid Mech.* **71**, 251–271.

FIÉVET, R., BAARS, W. J., SILVA, D. & TINNEY, C. E. 2013 High fidelity measurements in the far-field of a Mach 3 jet. *Bull. Am. Phys. Soc.* **58** (18), D24.00007.

GALLAGHER, J. A. & MCLAUGHLIN, D. K. 1981 Experiments on the nonlinear characteristics of noise propagation from low and moderate Reynolds number supersonic jets. *AIAA Paper* 1981-2041.

GEE, K. L. 2005 Prediction of nonlinear jet noise propagation. PhD thesis, The Pennsylvania State University, State College, PA.

GEE, K. L., DOWNING, J. M., JAMES, M. M., MCKINLEY, R. C., MCKINLEY, R. L., NEILSEN, T. B. & WALL, A. T. 2012 Nonlinear evolution of noise from a military jet aircraft during ground run-up. *AIAA Paper* 2012-2258.

GEE, K. L., SPARROW, V. W., JAMES, M. M., DOWNING, J. M., HOBBS, C. M., GABRIELSON, T. B. & ATCHLEY, A. A. 2008 The role of nonlinear effects in the propagation of noise from high-power jet aircraft. *J. Acoust. Soc. Am.* **123** (6), 4082–4092.

GRESKA, B., KROTHAPALLI, A., HORNE, W. C. & BURNSIDE, N. 2008 A near-field study of high temperature supersonic jets. *AIAA Paper* 2008-3026.

HALL, J. W., HALL, A. M., PINIER, J. T. & GLAUSER, M. N. 2009 Cross-spectral analysis of the pressure in a Mach 0.85 turbulent jet. *AIAA J.* **47** (1), 54–59.

HAMILTON, M. F. 2013 Effective Gol'dberg number for diverging waves. *J. Acoust. Soc. Am.* **134**, 4099.

HAMILTON, M. F. & BLACKSTOCK, D. T. (Eds) 2008 *Nonlinear Acoustics*. Acoustical Society of America.

HAMMERTON, P. W. & CRIGHTON, D. G. 1993 Overturning of nonlinear acoustic waves. Part 1. A general method. *J. Fluid Mech.* **252**, 585–599.

HOWELL, G. P. & MORFEY, C. L. 1987 Nonlinear propagation of broadband noise signals. *J. Sound Vib.* **114** (2), 189–201.

KERHERVÉ, F., FITZPATRICK, J. & JORDAN, P. 2006 The frequency dependence of jet turbulence for noise source modelling. *J. Sound Vib.* **296**, 209–225.

KUO, C. W., VELTIN, J. & MCLAUGHLIN, D. K. 2010 Effects of jet noise source distribution on acoustic far-field measurements. *AIAA Paper* 2010-474.

KUO, C.-W., VELTIN, J. & MCLAUGHLIN, D. K. 2012 Effects of jet noise source distribution on acoustic far-field measurements. *Intl J. Aeroacoust.* **11** (7–8), 885–915.

LAUFER, J., SCHLINKER, R. & KAPLAN, R. E. 1976 Experiments on supersonic jet noise. *AIAA J.* **14** (4), 489–497.

LIGHTHILL, M. J. 1954 On sound generated aerodynamically. II. turbulence as a source of sound. *Proc. R. Soc. Lond.* A **222** (1148), 1–32.

MCINERNY, S. A. 1996 Launch vehicle acoustics part 2: statistics of the time domain data. *J. Aircraft* **33** (3), 518–523.

MCINERNY, S. A. & ÖLÇMEN, S. M. 2005 High-intensity rocket noise: Nonlinear propagation, atmospheric absorption, and characterization. *J. Acoust. Soc. Am.* **117** (2), 578–591.

MCLAUGHLIN, D. K., BRIDGES, J. E. & KUO, C. W. 2010 On the scaling of small, heat simulated jet noise measurements to moderate size exhaust jets. *AIAA Paper* 2010-3956.

MCLAUGHLIN, D. K., MORRISON, G. L. & TROUTT, T. R. 1975 Experiments on the instability waves in a supersonic jet and their acoustic radiation. *J. Fluid Mech.* **69**, 73–95.

MORFEY, C. L. & HOWELL, G. P. 1981 Nonlinear propagation of aircraft noise in the atmosphere. *AIAA J.* **19** (8), 986–992.

MORRIS, P. J. 1977 Flow characteristics of the large scale wave-like structure of a supersonic round jet. *J. Sound Vib.* **53** (2), 223–244.

NAGAMATSU, H. T. & HORVAY, G. 1970 Supersonic jet noise. In *8th Aerospace Sciences Meeting*, AIAA.

NAUGOL'NYKH, K. A., SOLUYAN, S. I. & KHOKHLOV, R. V. 1963 Spherical waves of finite amplitude in a viscous thermally conducting medium. *Sov. Phys. Acoust.* **9** (1), 42–46.

NORUM, T. D. & SEINER, J. M. 1982 Broadband shock noise from supersonic jets. *AIAA J.* **20** (5), 68–73.

PAPAMOSCHOU, D. & DEBIASI, M. 1999 Noise measurements in supersonic jets treated with the Mach wave elimination method. *AIAA J.* **37** (2), 154–160.

PAPAMOSCHOU, D., MORRIS, P. J. & MCLAUGHLIN, D. K. 2010 Beamformed flow-acoustic correlations in a supersonic jet. *AIAA J.* **48** (10), 2445–2453.

PESTORIUS, F. M. & BLACKSTOCK, D. T. 1974 Propagation of finite-amplitude noise. In *Finite-Amplitude Wave Effects in Fluids, Proceedings of the 1973 Symposium*, pp. 24–29. IPC Science and Technology Press.

PETITJEAN, B. P., VISWANATHAN, K. & MCLAUGHLIN, D. K. 2006 Acoustic pressure waveforms measured in high speed jet noise experiencing nonlinear propagation. *Intl J. Aeroacoust.* **5** (2), 193–215.

PHILLIPS, O. M. 1960 On the generation of sound by supersonic turbulent shear layers. *J. Fluid Mech.* **9**, 1–28.

POTTER, R. C. 1968 An investigation to locate the acoustic sources in a high speed jet exhaust stream. *TR*-68-4. Wyle Laboratories.

POTTER, R. C. & CROCKER, M. J. 1966 Acoustic prediction methods for rocket engines, including the effects of clustered engines and deflected exhaust flow. *Contractor Rep.* 566. NASA.

SAXENA, S., MORRIS, P. J. & VISWANATHAN, K. 2009 Algorithm for the nonlinear propagation of broadband jet noise. *AIAA J.* **47** (1), 186–194.

SEINER, J. M., BHAT, T. R. S. & PONTON, M. K. 1994 Mach wave emission from a high-temperature supersonic jet. *AIAA J.* **32** (12), 2345–2350.

TAM, C. K. W. 1995 Supersonic jet noise. *Annu. Rev. Fluid Mech.* **27**, 17–43.

TAM, C. K. W. 2009 Mach wave radiation from high-speed jets. *AIAA J.* **47** (10), 2440–2448.

TAM, C. K. W. & CHEN, P. 1994 Turbulent mixing noise from supersonic jets. *AIAA J.* **32** (9), 1774–1780.

TAM, C. K. W., GOLEBIOWSKI, M. & SEINER, J. M. 1996 On the two components of turbulent mixing noise from supersonic jets. *AIAA Paper* 1996-1716.

TAM, C. K. W. & HU, F. Q. 1989 On the three families of instability waves of high-speed jets. *J. Fluid Mech.* **201**, 447–483.

TAM, C. K. W., VISWANATHAN, K., AHUJA, K. K. & PANDA, J. 2008 The sources of jet noise: experimental evidence. *J. Fluid Mech.* **615**, 253–292.

TANNA, H. K. & DEAN, P. D. 1975 The influence of temperature on shock-free supersonic jet noise. *J. Sound Vib.* **39** (4), 429–460.

TENNEKES, H. & LUMLEY, J. L. 1972 *A First Course in Turbulence*. The MIT Press.

TINNEY, C. E., UKEILEY, L. S. & GLAUSER, M. N. 2008 Low-dimensional characteristics of a transonic jet. Part 2. Estimate and far-field prediction. *J. Fluid Mech.* **615**, 53–92.

TROUTT, T. R. & MCLAUGHLIN, D. K. 1982 Experiments on the flow and acoustic properties of a moderate-Reynolds-number supersonic jet. *J. Fluid Mech.* **116**, 123–156.

VARNIER, J. 2001 Experimental study and simulation of rocket engine freejet noise. *AIAA J.* **39** (10), 1851–1859.

VELTIN, J., DAY, B. J. & MCLAUGHLIN, D. K. 2011 Correlation of flowfield and acoustic field measurements in high-speed jets. *AIAA J.* **49** (1), 150–163.

VISWANATHAN, K. 2004 Aeroacoustics of hot jets. *J. Fluid Mech.* **516**, 39–82.

VISWANATHAN, K. 2006 Instrumentation considerations for accurate jet noise measurements. *AIAA J.* **44** (6), 1137–1149.

VISWANATHAN, K. 2008 Does a model-scale nozzle emit the same jet noise as a jet engine? *AIAA J.* **46** (2), 336–355.

WEBSTER, D. A. & BLACKSTOCK, D. T. 1978 Experimental investigation of outdoor propagation of finite-amplitude noise. *Contractor Rep.* 2992. NASA.

WITZE, P. O. 1974 Centerline velocity decay of compressible free jets. *AIAA J.* **12** (4), 417–418.